IPP-Report

Max-Planck-Institut für Plasmaphysik

Bauer, Alexander

Characterisation of a Particle Injector for ASDEX Upgrade and Simulation of the Particle Trajectories in the Plasma Edge

IPP 2018-23
November 2018


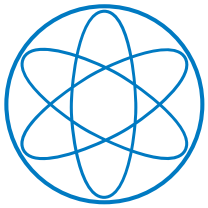


Master Thesis in Physics at
Technische Universität München

Characterisation of a Particle Injector for ASDEX Upgrade and Simulation of the Particle Trajectories in the Plasma Edge

presented by

Alexander Bauer

Garching, 17.09.2018

First Promoter: Prof. R. Neu

Second Promoter: Prof. U. Stroth

Supervisor: Dr. V. Rohde

Abstract

Dust is a problem of future fusion devices. The plasma facing components (PFCs) are eroded by several mechanisms as sputtering or arcing. This leads to the creation of atomic W or W particles with sizes up to 100 μm and velocities up to 100 m s^{-1} in the scrape off layer. Dust can be transported into the core plasma or deposited on the vessel surfaces. It leads to impurities in the plasma influencing the plasma operation and hindering the ignition of the plasma. Especially the high-Z material tungsten (W) used for PFCs of fusion devices has a large influence on the core plasma. Therefore, the creation of the dust as well as the penetration into the core plasma have to be investigated.

This thesis describes the characterisation and integration of a particle injector from the Korean tokamak KSTAR into the tokamak ASDEX Upgrade at the MPI for Plasma Physics in Garching to study the penetration and effect of macroscopic particles on the plasma. In comparison to the characterisation done in Korea the characterisation is additionally performed under vacuum conditions. Small, defined amounts of different kinds of W dust can be injected into a plasma discharge to study the evolution of the core W concentration and to follow the particle trajectories. Knowing the characteristics of the injector and the powder the penetration probability can be calculated and the behaviour of the plasma after injection can be evaluated.

The injector characteristics are used as initial parameters for trajectory simulations with the DUCAD code. These give an indication of the penetration depth and allow to estimate how the particle trajectory will be influenced by the plasma. These simulations performed with different grain sizes and velocities showed deeper penetration with increasing size and velocity. The comparison of simulation and future experiments will provide data to improve the modelling of dust which could enable to make predictions for future fusion devices.

Contents

Chapter 1

Introduction

In the recent past the decision regarding the future energy production went towards an environmental friendly and CO_2 neutral energy production to counteract and limit global warming. The rising global need for energy led to the search for alternative and environmental friendly ways of energy production to replace the current burning of fossil fuels. One step is to only use renewable energies, but they are depending on weather conditions and are not available everywhere. The needed energy cannot reliably be produced by renewable energies alone. In case of unfavourable conditions or high energy demand a backup is needed. Additionally, one either needs good storage devices to save overproduced energy, power plants not reliant on weather conditions or a mixture of both to guaranty a stable energy supply. These power plants would then operate as a base load and would work in synergy with renewable energies, backing them up when needed.

One possibility for a base load power plant could be fusion power plants [1]. A power plant of this kind is inherent save as a loss of power supply leads to a shut down of the power plant and end of the energy production. The amount of radioactive material in the device at every time is low and the fusion process does not allow an uncontrolled chain reaction. The fuel inside is only enough for a few seconds of operation. Tritium (T) is part of the fuel but it is only weakly radiating and produced inside the device. For the production of the T no additional facilities are necessary which limits the amount of material contaminated. As vacuum conditions are required the total amount of T in the device is about one gram, which could be released into the environment in case of an accident. However, there is more T in the device as explained later. Some of the in-vessel components will be activated but they are made from materials that only get weakly activated or form short lived isotopes only. This leads to short times until such a plant can be taken down after it is not used any more. No long term storage of the used components is necessary as many thousand years for fission products. After 100 years the radiation of the majority of the radioactive or activated material has decayed below the hands on limit [2]. The materials can then be reused.

Up to now there is no power plant of this kind and the processes relevant

for fusion reactors are still researched. A fully operational fusion power plant will take some time. The International Thermonuclear Experimental Reactor (ITER), currently under construction in Cadarache, France, will operate for the first time with fusion power being the major heating mechanism. ITER is planned to operate at $Q = 10$ [3]. which means that the the power from the fusion reaction is ten times that of the additional heating power required to maintain the plasma temperature. With this reactor no ignition of the plasma is reached which would equal to $Q = \infty$. It will gather the necessary information allowing to run a fusion power plant. It should also show that the concepts and designs for fuelling, sustaining operation for long times and energy gain are realised.

The process used in an operating power plant is nuclear fusion, the same process running in the sun to generate energy. As the conditions of the core of the sun cannot be realised on the earth as the gravitational pressure is beyond reachable ones on the earth one adapts this process by using magnetic forces. The main process of the sun is pp fusion. The fusion process in the sun has a low reaction rate but in the large volume and at high densities results in a large energy output. On earth a faster reaction with high fusion rate in a magnetically confined volume is used. The fusion rate for different fusion reactions are shown in 1.1. The fusion rate of the pp reaction is several orders of magnitude lower than those shown. The reaction applied in a fusion reactor will be the fusion of deuterium (D) and T. It runs at lower pressure but higher temperature with a high cross section to allow an efficient reaction rate and energy output. The produced helium (He) will be used to heat the plasma. High temperatures are needed to be around the maximum of the fusion rate and to overcome the coulomb barrier to fuse D and T as they have the same sign of charge. At the high temperatures atoms are ionised and form a plasma. This plasma then contains only negatively charged electrons and the positively charged atom cores and allows to confine it magnetically.

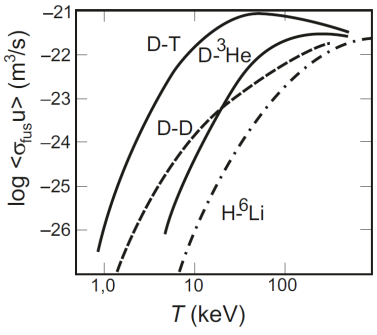

FIGURE 1.1: The plot depicts the fusion rate of different fusion reactions as a function of the temperature. Picture taken from [4].

To achieve the ignition of a plasma the Lawson criterion sets a threshold for an ideal plasma. The ignition of the plasma means that the heating from the fusion products comes up for all energy losses of the plasma.

$$n \cdot T \cdot \tau_E > 3 \times 10^{21} keVsm^{-3} \tag{1.1}$$

The plasma quantities in the criterion in equation 1 are n, T and τ_E which denote the plasma density, plasma temperature and the energy confinement time. This triple product is derived from the Lawson criterion. This leads to necessary values for these parameters of $2 \times 10^{20}\,\mathrm{m}^{-3}$, 15 keV and 3 s confinement time [4] to obtain plasma ignition for a mixture of D and T fuel. The threshold gets influenced by changing impurity concentrations in the core plasma [5]. In a realistic fusion device impurities will cause additional losses, which changes the necessary values of n, T or τ_E of the criterion as shown in figure 1.2. Therefore, the impurity concentration needs to be very low as otherwise a plasma ignition or burning plasma cannot be realised.

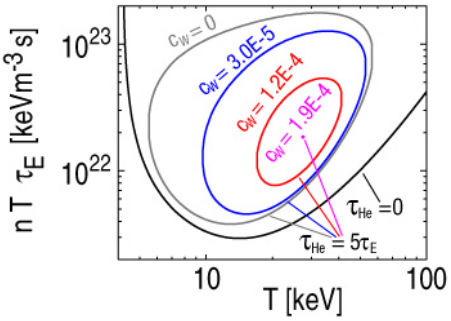

FIGURE 1.2: Shown are the values of the triple product necessary for the ignition of the plasma as a function of the temperature. Ignition can be achieved in the ideal case above the solid black line. Additional impurities as He which is the product of the fusion reaction or W restrict the ignition to parameters enclosed by the lines. With increasing W concentration the possible parameter range decreases. Picture taken from [5].

Impurities originate from the fusion reaction as He or from eroded material inside the vessel transported or diffused into the core. The impurity content must be held low to allow operation of the plasma in a fusion power plant which requires understanding of the creation of dust as well as the transport mechanisms. Therefore, dust and dust creating processes are studied by analysing dust collected inside the machine and dust particles are artificially brought into the plasma to study its impact.

This thesis focuses on the characterisation, commissioning and integration of a powder injector into ASDEX Upgrade (AUG) that was used at the Korean tokamak experiment KSTAR [6, 7]. The injector can be utilised to study the tungsten (W) penetration and impact on the plasma behaviour. This is done by injecting known amounts of tungsten with a known velocity. The knowledge of these parameters and the size of the particles allows for a detailed analysis of the transport and the impact on the plasma performance. The results of the characterisation are used as input parameters for investigations with the

DUCAD (DUst Characterisation And Dynamics) transport code. It is applied to simulate how dust particles with the given properties behave for an injection into the plasma.

This thesis is structured as follows: chapter 2 provides information about the dust formed in fusion devices and the impact of dust on the operation of those devices. In chapter 3 the injector and its functionality are described. The setup used for the characterisation of the injector is part of chapter 4. The results of the characterisation of the injector are discussed in chapter 5. Chapter 6 reports on simulations of particle trajectories using the results of the characterisation as input parameters for the DUCAD code.

Chapter 2

Dust in fusion devices

2.1 Impurity sources and issues

One major concern for the operation of future power plants is dust formed inside the machine. The creation mechanism as well as the formed amounts of dust are intensively studied due to their impact on the performance of a fusion device, the edge and core plasma.

Dust is eroded material from plasma facing components (PFCs). It can be redeposited on PFCs forming layers or transported into the core plasma. With increasing thickness of these deposited layers, they become unstable by internal stresses and flake off forming dust. Dust particles can deposit in hard to access locations where they accumulate and built up an in vessel inventory of dust.

Dust creation will be an increasing problem as the machines are getting bigger with longer duty cycles and with higher particle and power fluxes [8, 9] on the PFCs. The eroded amount increases leading to more dust in the machine building up with operation time.

The PFCs will be continuously eroded during plasma operation with different rates for a low-Z material as carbon (C) or a high-Z material like W. Whereas low-Z materials are strongly sputtered even by D, high-Z materials as W can only be sputtered by impurities as they have enough energy to overcome the sputter threshold. As the sputter yield for W is quite low, other processes as arcing can play a role in the erosion. Arcs, which are observed at some regions in all present day fusion devices [8, 10, 11, 12], cause local melting of the PFCs, which leads to the production of droplets with typical diameters of some microns. Furthermore, macroscopic particles can be formed by local melting due to high heat loads.

These erosion processes create dust particles with a size ranging from a few 10 nm to a few 100 μm [13, 12]

Dust particles are created with velocities ranging from a few to 100 $\mathrm{m\,s^{-1}}$ [10, 12, 14, 15]. Some particles are observed with higher velocities [16, 17, 18] of up to 500 $\mathrm{m\,s^{-1}}$. Depending on their angle towards the surface they leave the PFCs towards the plasma. Others are deposited on the wall again.

The difference of the influence of low-Z and high-Z materials on the core plasma are the different amount and origin of radiation and the resulting energy losses. Low-Z elements get fully ionised in the core plasma and are only emitting bremsstrahlung which is a lesser concern. High-Z materials as W do not get fully ionised and bremsstrahlung is only a minor contribution. High-Z materials emit line radiation with a large radiative efficiency [19] and lead to energy losses by cooling the core plasma [5]. This sets an upper limit of W in the plasma.

Further, the formed dust inside the device is connected to safety and operational issues. The dust retains the fuels D and T and leads to higher consumption and an increase of the T inventory in the vessel causing operational issues and subsequently safety ones. As mentioned before only little amounts of fuel are meant to be in the machine but this retention increases the amount significantly. A higher T retention leads to an increased radioactive inventory that can be released in case of an accident. At an incident with air or water getting into the vacuum vessel the stored hydrogen with the oxygen may form explosive mixturess [8, 9, 20]. An explosion would distribute present activated dust in the environment, which is a main concern, and lead to damage of the machine. As a consequence the maximum allowed inventory of dust as well as retained T in ITER is limited [20, 21].

During early operation of the AUG tokamak its FPCs were made from C because it shows only little impact on the plasma and good thermal properties. Besides the positive aspect of low plasma influence and a higher critical amount for plasma operation than other elements, C exhibits a disadvantage in case of fusion operation. The C of the PFCs retains and stores significant amount of hydrogen by forming hydrocarbons removing it from the plasma inventory. With time an in vessel inventory builds up and the formation of hydrocarbons erodes the PFCs. Those erosion processes also lead to the formation of deposit layers with the issues as mentioned before. The hydrocarbons can get pumped out by the vacuum pumps resulting in the loss of the reactor fuel or deposit in hard to access areas and accumulate in the vessel. Whereas the pumped out portion can be recycled, the hydrogen bound in layers and dust in the machine is problematic as discussed before.

This led to the change from C as wall material to W. W shows significantly lower hydrogen retention but does not get ionised fully as mentioned before. W shows an extremely high melting point and low erosion yields which makes it a good choice for the PFCs.

After the change from C to W the formed dust in the vessel was investigated at vent events at AUG. Dust collection showed a significant amount of macroscopic W particles and spheres hinting to a relevant W source in the machine.

2.2 Dust studies at ASDEX Upgrade

For C PFCs deposit layers can form and strong erosion occurs with the connected issues as mentioned before.

With the transition to high-Z PFCs these issues could be reduced but the effect of the then formed dust needed to be investigated. The concentration of these high-Z materials in the core is critical as mentioned before and must be limited to ensure plasma operation.

There are two mechanisms of W penetrating into the core region. Ions in the scrape off layer (SOL) created at the wall can drift and diffuse into the confined region and macroscopic particles penetrating the separatrix release their material in the confined region where it diffuses into the core. For some discharge conditions W accumulation in the core is observed which leads to high energy losses and cooling of the plasma [22]. The W profile in the core is connected to the turbulent and neoclassical transport of W in the core and pedestal region [23]. Strong peaking of the core W density occurs when the neoclassical transport dominates [22] in unfavourable condition of inward neoclassical convection [23]. When W is transported towards the core plasma radiation in the core increases. The central W content can be controlled using central electron and ion cyclotron resonance heating [22, 23]. As single W grains can contain large numbers of W atoms they have strong local and temporal effects on the plasma and on the core. They are transported into the core when favoured by the discharge conditions as mentioned before or the amount of W is large.

Macroscopic particles have a higher probability to penetrate into the core plasma. The core W content is, therefore, connected to the probability of particles to penetrate beyond the separatrix. If created particles have a high probability to release W close to the separatrix the control of dust needs to be addressed and is critical for the operation. Therefore, the central W content is linked to the amount of dust created as well as the size and velocity.

The core limit for the W concentration in AUG is at fraction of 1×10^{-4} of the plasma density which is around $7 \times 10^{19}\,\mathrm{m}^{-3}$ in typical D discharges. The limit for other impurities is different but for the test reactor ITER the W limit is around 1×10^{-5} [5]. Therefore, the mechanism of W transport need to be understood. W in the SOL can alter the plasma properties in this region. The interaction of W with the divertor leads to higher sputtering compared to other impinging species as W is impinging on a W surface.

After the transition intensive studies of the dust found in AUG were performed to evaluate the dust creation as well as the size and composition of the dust. This was done by placing silicon wafers in the machine to collect particles during operation. After a campaign they were removed and an automated analysis using scanning electron microscopy (SEM) and energy dispersive X-ray spectroscopy (EDX) to classify the dust particle size and composition was applied [13, 10, 24].

Dust particles consist mainly of W but also C and boron (B) contributions

are present. The elemental contribution to the particles can be explained by the operation and the elements present in the machine.

Apart from the composition of the particles another point is the size and shape of the particles as well as the number of them. Investigations [13, 24, 25] showed the shape of the collected particles separated into two classes. On the one hand spherical particles and on the other hand irregularly shaped particles containing W, C and B. The particles range from some nm to 100 μm. The typical size of spheres found is around 1 μm.

The mass of the collected dust can be used for an extrapolation of the mass of the dust created in the whole vessel. This is a rough estimation and only allows to see a tendency of the total mass. The mass is several 100 mg per measurement interval [10, 13, 25] between vent events at AUG. For other machines the collection of dust showed masses of several 100 mg so some 10 g also including dust collected from underneath vessel components [26, 27]. This mass is not critical for AUG or other devices but for future devices it will most likely be as the plasma time at AUG is around 4000 s a year whereas ITER will have single discharges of up to and over 1000 s [28] leading to a higher dust creation rate and faster accumulation of the dust [9].

Dust particles are created by different mechanisms as mentioned before. Arcing is one major creation mechanism [29]. In AUG it is strongly dependent on the toroidal as well as the poloidal position [30]. The W spheres found close to arc traces are similar in size and shape to those in the collected dust. This makes it plausible that the W spheres found are droplets resulting from arcing processes also because they show no contamination of other impurities [10, 30]. Another characteristic of arcing along with erosion is the creation of droplets with a velocity towards the plasma [30]. Depending on the size and velocity the penetration into the core plasma beyond the separatrix has different probabilities.

One main disadvantage of the dust collection is that dust is gathered over a whole campaign and does not allow to identify the creation mechanism of the dust. There are several in-situ methods to observe the dust, dust creation events or collect particles during operation [12, 18].

One of those techniques is the analysis of camera recordings from inside the device [31, 32, 33, 34]. From those recordings properties as speed and creation location can be obtained. The observation of dust is limited because only large enough particles are observed. Additionally, particles do not start to glow instantly and are not visible where they have been created except they directly originate from melting processes. Particles are only observable when they have a diameter of 3 to 5 μm and a temperature of above 1500 K, hence, the emitted radiation is high enough for detection by a camera and higher than the surrounding plasma [35, 34].

The penetration and the effect of artificially introduced dust on the plasma can be studied. To investigate the penetration of dust, a small known amount is injected in the SOL with a defined speed. By monitoring the central tungsten concentration via spectroscopy, the penetration probability can be calculated.

To study the transport and impact of dust particles simulations are applied. Those rely on precise input data. For intrinsic dust observed by camera several parameters are unknown which leads to uncertainties in the calculation. Especially the size and the composition of observed particles are unknown and have large influence on the result. This lead to the usage of dust injectors of different kinds to have control over the initial parameters of the dust [6, 36, 37, 38, 39]. Exact knowledge of the injector is obtained by characterising it. These characteristics can be used as input parameters for the codes in order to validate the code with injector experiments. When an exact modelling is possible the simulation can also be applied to model future devices and predict the impact of impinging dust.

Chapter 3

Injector setup

To study the effect of dust on the SOL plasma and the penetration into the core plasma, known amounts of dust are injected into a plasma discharge. The injector cannot only be used to study the effect of dust on the plasma but its injection characteristics can also be used as input parameters for simulations.

In the following the injector used for the later characterisation is described and its functionality is explained.

The injector setup was developed at the Korea Advanced Institute of Science and Technology KAIST for the operation in the KSTAR tokamak [7]. The injector, therefore, fulfils the requirements for the operation in such an environment. It is supplied from the Korean tokamak experiment KSTAR.

3.1 Criteria for motor and materials

The injection device consists of two essential parts, the motor with its control and the injector.

On the one hand motor and injector must be able to operate under vacuum conditions which sets limitations on the materials used, see also [7] part II.A. and II.B. This means that the outgassing of the motor and injector components in vacuum must be low. On the other hand, the motor must operate under high magnetic fields of around 2 to 3 T. This makes it impossible to use an electrical motor. A third point is the ability to work without cooling as no active cooling is applied to the motor and injector. The motor itself is not directly exposed to the plasma as a W-coated graphite cap protects the motor and injector. By positioning the injector behind a limiter the temperature will not exceed 100 °C which can be monitored by an IR camera close by. Only the tip of the injector penetrating the cap can have direct plasma contact visible in figure 5.20.

These limitations and necessities lead to the choice of a rotary piezo motor, the model PUMR-40 from piezo-tech [7] . The vacuum compatibility of motor and injector was tested and confirmed with the operation under vacuum conditions. It was operated in a glow discharge with mounted protection cap without any detectable damage to the motor, injector or the protection

cap. Dedicated experiments under high magnetic fields were not performed. Experiments with low fields were done without impact on the injector. The successful operation during the characterisation at KAIST and in KSTAR under high magnetic fields with the same injector shows the ability to operate under these conditions.

For the injector the same requirements for the material and operation apply. The parts of the injector are made of stainless steel [7].

3.2 Injector parts and setup

The device consists of an injector with a magazine filled with dust. The motor pulls back a piston and compresses a spring. Meanwhile dust is supplied from the magazine to the piston. Then the piston is released, the spring accelerates the piston and the powder is injected.

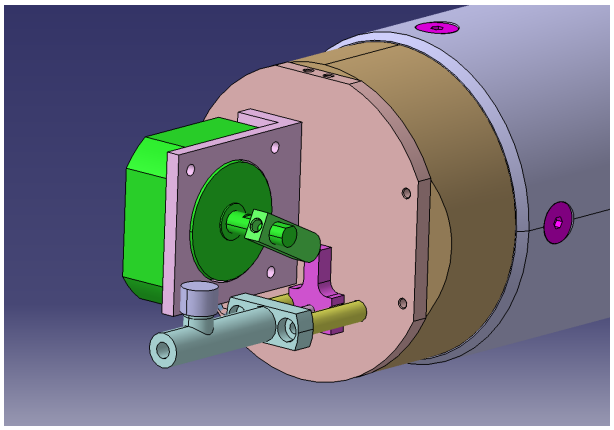

FIGURE 3.1: The motor is shown in green with the bar mounted on the shaft of it. The motor runs in counter clockwise direction. The injection gun is shown in light blue and the trigger in purple. Towards the front of the injection gun the magazine in purple is placed. The injector is mounted on the midplane manipulator on the connector in silver on the right.

The injector shown in figure 3.1 consists of three main parts the injection gun, a moveable piston with trigger and a magazine [7]. The injection gun is the core part of the injector. At the front of the injection gun the cylindrical magazine is situated storing the powder for the injections. In the centre is a small hole where the powder can fall through to supply powder to the piston. The magazine holds the powder for over 40 injections. The piston is located inside the injection gun. It has two holes drilled into it. One is drilled from the front in axial direction with a diameter of 6 mm and the second one is on top. This is visualised in figure 3.2a.

On the shaft of the motor a bar with a round end is attached. The bar transfers the rotation of the motor and pushes the trigger back which then pulls back the piston.

A compression spring is located inside the injection gun. It is confined by the thick front part of the piston and the end of the injection gun.

When the piston gets moved back the spring gets compressed and builds up elastic energy. The built up energy propels the piston to inject the dust when the bar moves past the trigger and releases it. The forward motion of the piston is stopped by the trigger hitting the back of the injection gun. The powder is thrown out as it keeps its gained momentum. The different positions of the piston during one injection and the loading process are illustrated in figure 3.2.

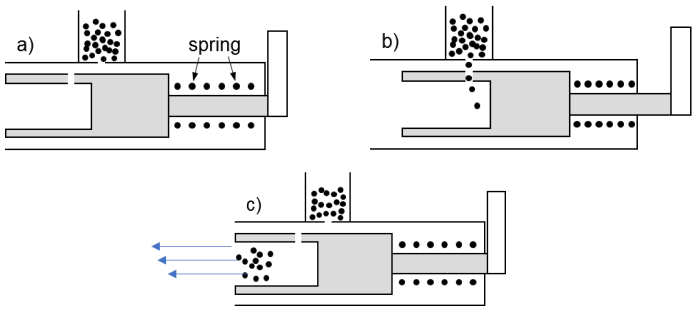

FIGURE 3.2: Picture (a) shows the initial state when the motor is at rest. The magazine on top of the injection gun. Inside of the injection gun the piston (grey) with the cavity for the powder at the front (left) is located. The spring (symbolised by the dots) is placed in the injection gun around the thinner part of the piston. At the back (right) of the piston the trigger is mounted. The motor starts moving and the bar pushes back the trigger with the attached piston. This allows the powder to fall into the cavity of the piston to load the powder (b) during the time the hole in the magazine and the piston are above each other. Once the bar releases the trigger, the piston is accelerated by the spring. The powder is thrown out when the piston is stopped by the trigger hitting the injection gun in (c).

The injector and the motor are mounted on a base plate. The dimensions of the device with the mounted protection cap are 8.3 cm by 8.3 cm for the base plate and a height of 7 cm with the cap mounted. The base plate also acts as connector to install the injector at the midplane manipulator (MEM) which is the installation position for the experiments in AUG. It can be seen in figure 3.1 on the right side. The installation position is illustrated in figure 5.1 and the installed injector with mounted protection cap is shown in figure 5.20.

3.3 Motor control

In order to control the injector, the motor rotation and the connected bar position must be controlled. This can be done in two ways.

The first option is to control the motor via a PC based software that allows to change all running parameters of the motor as well as starting and stopping the rotation of the motor. The software allows to set the running speed of the

motor and the run time. The PC is connected to the motor controller directly by a USB connection. The motion can be stopped at any point by pressing the respective button.

The used motor does not have an encoder to track the motor position. The motor position is controlled by setting two parameters, run time and running speed. In conjunction with the later experiments a run time of 600 ms for one revolution is chosen. The running speed is connected to the amount of powder supplied from the magazine to the piston in the time the holes are on top of each other.

The experiments and tests showed that after 10 to 20 injections the bar has changed its position by a quarter turn. Some optimisations of the injector decreased the position shift per injection and resulted in these values. Therefore, this effect is still present and noticeable for multiple consecutive injections. After 20 or more injections the effect of accumulating powder inside the injector sometimes increases this effect. This limits the number of injections to about 25 injections before an enhanced probability for a malfunction arises.

The problem of not knowing the current position could be solved by installing a reference switch to give a signal when the bar is at a specified position. This way it could be kept track of the position and more injections would be possible. The maximum number of injections is then limited by the magazine capacity and the powder accumulation in the injection gun.

The second method of control is to trigger the motor by an external signal and not by PC. The parameters for the motor are set as mentioned above and saved on the controller. The motor runs with the set properties when triggered by the external signal. The external control is established by an connection port on the motor controller for the external trigger signal. The trigger signal allows a timed and synchronised usage of the injector to the plasma discharge and the other diagnostics. To connect the PC outside the experiment hall and the motor controller inside the experiment hall the signal leaving the PC via the USB port is converted into a LAN signal and back to USB. A sketch of the wiring is shown in figure 3.3. This allows to change the running parameters at any time if a change of parameters is necessary. Making changes to the running characteristics is problematic as the motor position can not be seen. The operation of the motor and therefore of the injector is based on the identified characteristics of the motor.

The second method is the one employed for the operation in AUG because of the synchronisation of the injection with the other diagnostics. This is done by the AUG timer module [40]. For the laboratory experiments the first method is used as no synchronisation is needed. The external triggering of the motor was successfully tested in the laboratory as well as the connection of the PC outside the experiment hall and the motor controller inside.

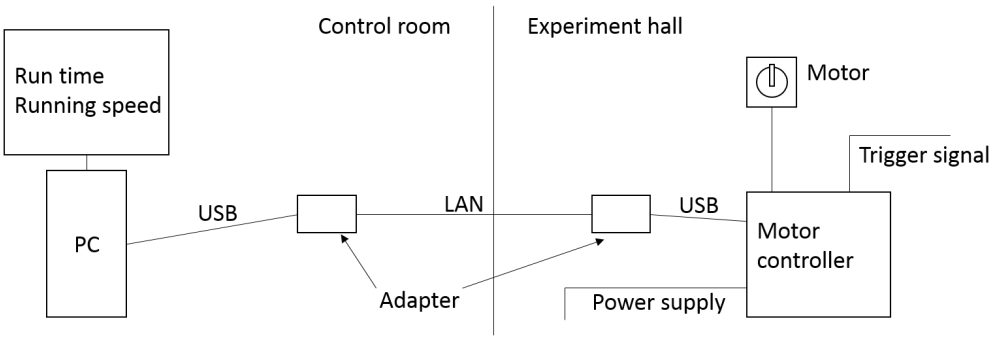

FIGURE 3.3: The sketch shows the wiring to set the parameters and control the motor during the experiment. The control starts with setting the run time and running speed by the software on PC. The signal of the software uses the USB port for connection to the motor controller. The distance from outside the experiment hall to the motor in the experiment hall is overcome by a LAN connection. Two adapters are used to convert to a LAN signal and then back to USB to establish the connection to the controller. For synchronisation with diagnostics the motor is triggered by an external signal.

Chapter 4

Characterisation setup

To evaluate the injection characteristics is the next step before integrating the injector into AUG. The injections are recorded with a high speed camera at atmospheric pressure and under vacuum. The analysis of the recordings gives insight on the injection characteristics as powder speed, range and spread of the particle cloud. Further, those experiments show the reliability of the device. In the following the measurement setup used for the recordings of the characterisation is described.

Under atmospheric pressure the powder is affected by air flows or eddies as seen on recordings made in the laboratory shown in figures 4.3a and 5.15. These additional influences alter the shape and behaviour of the dust cloud of the injected particles. This is especially relevant for longer times after the injection when the dust cloud gets thinner. Those influences by air can be almost excluded when the injections are carried out under vacuum conditions.

Due to the observed spread in air a characterisation of the injection is hardly possible. It is necessary to perform the characterisation under vacuum conditions to obtain precise properties of the injector. Further, the injector is operated in vacuum which makes it necessary to characterise it under vacuum conditions.

The carried-out experiments under vacuum conditions validate the capability of the motor and injector for vacuum operation that is needed for an operation in the AUG tokamak. These results confirm the findings in Korea with plasma injections and operation in KSTAR [6].

4.1 Vacuum chamber

Figure 4.1 shows the used vacuum vessel. The height is around 1 m and the diameter is about 80 cm. The pumps employed are two scroll pumps and two turbo molecular pumps. First ones are necessary to reach the pressure range in which the turbo molecular pumps can operate. When a pressure of below 100 Pa is reached the turbo pumps are switched on in addition. This two stage pump setup allows to reach pressures below 1×10^{-4} Pa, i. e. the influence of air on the injection and the dust cloud can be excluded.

The chamber has multiple ports that can be equipped with windows allowing to look into the chamber. They are utilised to monitor the injection with a fast camera and to provide the necessary illumination of the powder.

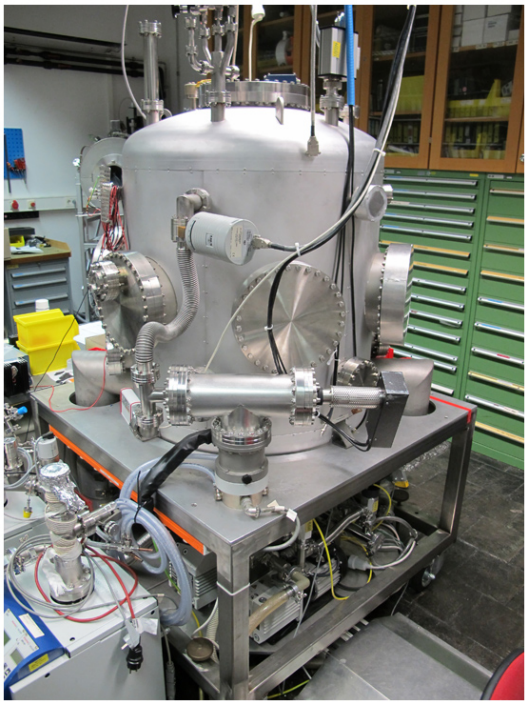

FIGURE 4.1: Shown is the vacuum chamber used for the experiments. The port on the left is replaced by a window and the camera is placed in front of it. The laser is placed in front of the port seen on the right. Picture taken from [41].

A description of the measurement and recording setup is given in the next section.

4.2 Measurement setup

The idea and basic principle behind the setup is to record the injected dust with a fast camera and analyse the recordings to deduce the different properties of the injection. From the evaluation of the recordings the characteristics and parameters of the injection and of the powder cloud are obtained. The properties of interest are the initial injection speed and the spread of the dust cloud of the particles. In a second step the shape evolution of the dust cloud can be derived.

The vacuum vessel is a core part of the measurement setup for the characterisation which can be seen in figure 4.2.

The chamber has a window at the front to mount and access the injector. It allows to monitor the injector and the injected powder inside. In front of this window the camera is placed. The placement of the injector in the vacuum

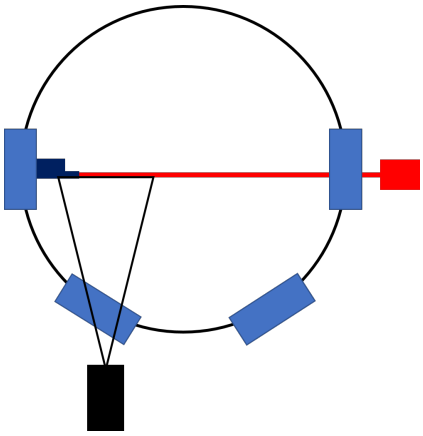

FIGURE 4.2: The scheme illustrates the recording setup viewed from above. It illustrates the setup and positioning of the different components but is not to scale. The distance of the camera (bottom, black) from the injection plane is around 50 cm. The laser (right, red) is positioned in front of the window on the right about 90 cm from the injector. The injector (dark blue) is mounted on the left. In blue the ports of the vessel are shown. The ones for the camera and the laser are equipped with windows and the others are sealed.

chamber has the drawback that the camera is further away from the injector than possible outside the chamber.

The camera used for recording is a Phantom V711, which allows to record with up to 7530 fps with full resolution of 1280 px × 800 px. The chip of the camera is about 50 cm away from the injection plane. A Nikon AF Micro-Nikkor 60 mm 1:2.8D objective is used for the recordings. It is positioned perpendicular to the laser and injection plane to record the light diffracted from the dust particles. The position of the camera is mostly fixed by the requirement to be perpendicular to the injection and laser as well as recording a large enough area where the dust is injected. Another important property limiting the observation is the amount of light diffracted by the dust that can be recorded. This favours a close placement of the camera.

Outside the vessel on the right of the camera the light source for illumination is located. A line laser is pointing at the injector through another window to illuminate the injected dust. This kind of laser device creates a laser line when projected on a wall. As shown in figure 4.2 the laser is aligned to the injection direction. The laser position is about 90 cm away from the injector. The laser device used is a 180LR from Fluke. The projected laser line has a width of 6 mm at the position of the injector. This is the size of the piston diameter.

The possible observable horizontal field of view is around 20 cm with the injector visible on the left of the recorded images. The vertical field of view is about 16 cm with the injector visible in the middle. Such pictures are shown in figures 4.3d and 5.11 which are converted to a size of 25.3 cm × 15.8 cm at the distance of the injector. For a recording with the injector in the vacuum

chamber the resolution is $0.198\,\mathrm{mm\,px^{-1}}$ and a frame rate of 500 fps is used. Recordings outside the vacuum chamber can have different resolution due to different distances from the camera to the injector.

4.3 Dust illumination

For initial investigations in air the illumination was done with bright halogen lamps connected to flexible light guides to focus the light on the injection plane. This provides good illumination in the volume in front of the injector. To enhance the contrast and minimise the background a black fabric was positioned behind the injector.

In the vacuum chamber a different method was needed as the halogen lamp could not be placed inside the vacuum chamber and a line laser was chosen. After validating this way of illumination in the laboratory under atmospheric conditions this was applied in the vacuum vessel. To reduce the background all lights in the lab were turned off and all windows of the vacuum vessel that were not needed were covered.

The advantage of the illumination by the halogen lamps is that the illumination is much brighter and the whole 3D cloud is visible. The cloud is transformed into a 2D projection of the cloud by the camera recording. The drawback is that particles in front or behind the focus of the camera are not recorded sharp. The line laser only illuminates one plane and therefore the recordings only show a 2D slice of the cloud where all recorded dust is sharp but showing smaller signal intensity. Dust that spreads or moves horizontally out of the laser plane is not observed but visible with the lamp illumination. This is a reason why there is no dust visible with the laser close to the injector compared to the halogen lamp. The dust is outside of the laser plane because of the spreading and influence of air flows in the laboratory on the cloud. With a larger injection angle

The effect of the spread due to a horizontal injection cone was found to be small compared to the observed spread of the dust cloud along the injection direction. The spread was determined in the laboratory at atmospheric pressure with a sheet of paper that was placed 15 cm below the injector to evaluate the impact region. The majority of the dust with the highest range was found on the paper within an angle of less than 6° towards both sides of the injector axis at ranges of around 17 cm. This shows that the observed spread is not due to a large spread of the injection angle but originates from the interaction with the air. The dust would be more spread at the farthest position if the injection angle would be the dominant factor.

A comparison of the illumination methods in the different environments is illustrated in figure 4.3.

With the lamp illumination in the laboratory in air shown in figure 4.3a more dust is seen compared to the laser illumination. This is especially evident in regions close to the injector some time after the injection when the dust

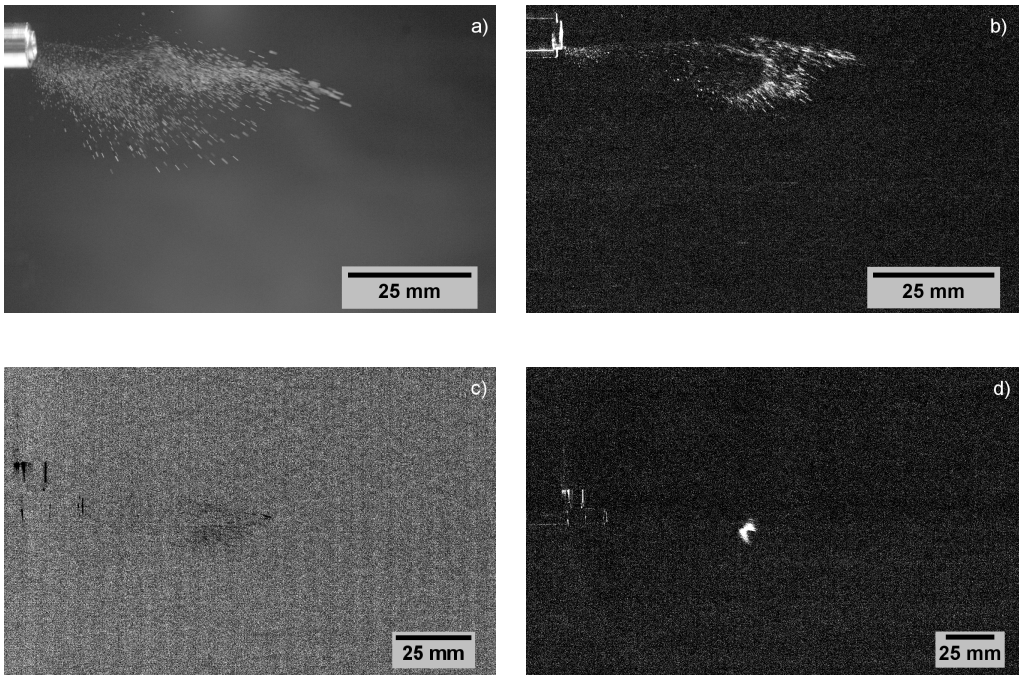

FIGURE 4.3: Comparison of the two illumination methods used in the laboratory with the halogen lamp in (a) and in (b) by the laser. The difference of the laser illumination in the vacuum vessel is shown for atmospheric pressure in (c) and for vacuum in (d). All pictures are taken 50 ms after the injection. The contrast of pictures with the laser illumination (b,c,d) was enhanced for better visibility. Pictures (a) and (b) have a field of view of 10.6 cm × 6.6 cm, (c) of 16.3 cm × 10.1 cm and (d) of 25.3 cm × 15.8 cm. The pictures show the full recorded image with a resolution of 1280 px × 800 px except for (c) which is only a 820 px × 512 px section. Pictures (c) and (d) can be found in figure 5.16 and 5.19 with different contrast, respectively.

cloud is spread and faint. In this case only the front parts of the dust cloud are illuminated by the laser as seen in figure 4.3b. To evaluate the speed the information is sufficient in some recordings but to determine which portion of the dust reaches the necessary ranges especially in air the laser illumination does not provide enough information. For injections with atmospheric pressure in the chamber shown in figure 4.3c the laser illumination shows a lower signal compared to the laboratory case which is due to the larger distance of the laser from the injector. This leads to limited identification already shortly after injection. Observation is already hardly possible around 50 ms after the injection or around 6 cm from the injector. The bad visibility of the dust in the chamber under atmospheric pressure is especially relevant for longer times after the injection when the dust cloud gets thinner.

Under vacuum conditions as shown in figure 4.3d the signal with laser illumination is much better indicating a denser cloud due to the smaller noticeable

spread and higher signal intensity. The recording in vacuum can be well evaluated over the whole time interval of the recording until the dust leaves the field of view.

The tests under vacuum are necessary and beneficial for a precise determination of the characteristics and for the demonstration of the operation in vacuum.

Chapter 5

Injector characterisation

5.1 Characterisation motivation

Prior to the integration into AUG the injection system needs to be characterised. It is essential that the injector works reliably before the device is mounted on the MEM. Further, there are several requirements for the injector to be met before the device can be installed.

The exact knowledge of the injection properties is also important to simulate and calculate the transport and trajectories of the dust after the injection.

It is important to ensure that the powder reaches the separatrix position. Due to the mounting position at the MEM an injection range of at least 10 cm is needed. Results of simulations shown later will evaluate whether this distance is reached in plasma or not.

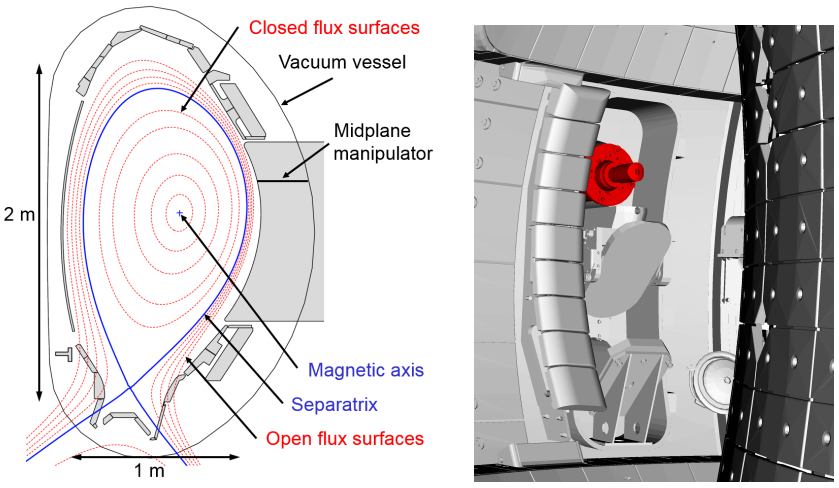

FIGURE 5.1: On the left the installation position of the injector on the MEM is shown in a poloidal cut of AUG with a typical plasma shape. The injector is located in the shadow of a limiter. The distance from the separatrix (blue) will be about 10 cm. The picture on the right shows the injector position (red) as seen by a fast camera used for monitoring and recording the injection.

Additionally, the initial injection speed is necessary to be measured. This provides the trajectory of the particles in vacuum. The speed is important to know as it has a strong effect on the penetration depth which controls the location where the grains evaporate and release W. This will also be investigated in the simulations presented later. Further, most of the powder should get close to the separatrix position which requires knowledge about the shape and evolution of the powder cloud after injection. This is important to show how the powder is distributed. Other parameters of the injector are the mass per injection, the grain size and shape of the powder. The information of the mass is necessary to allow the calculation of the penetration probability from the comparison with the measured W content. The properties of the powder like grain size and its distribution are necessary as different sizes presumably have different effects on the plasma and behave differently when in contact with the plasma.

With these properties a qualitative and possibly quantitative analysis of the results from experiments with plasma injection can be obtained.

In the following the analysis of these parameters is given performed with the setup described before. The methods applied are given, too. There were two injectors available called Injector A and Injector B. For the experiments at AUG Injector A is proposed as initial investigations showed that the injected mass by Injector B is significantly higher which may cause unduly high W concentration after injection. From a mechanical point of view Injector B is structurally almost identical to Injector A. Small differences are the diameter of the moving piston and the holes in the magazine and the piston.

5.2 First characterisation and pre-experiment adjustments

Before performing injection experiments in vacuum or recording injections, the reliability of the motor and the injector needed to be established and ensured. In this phase slight optimisations were made to the injector to obtain a smoother running and less friction between the moving parts of the injector. For example, at the interface of the trigger and the guides material was removed and the interface where the rotor pushes and slides over the trigger was polished.

The stopping or slow down due to dust remaining in the injector could be reduced and almost excluded. Mainly because the reduction of friction allows the motor to reliably overcome additional friction due to powder inside. The motor operates the injector even in the case that dust has been deposited inside the injector which is the case after multiple injections. This deposition cannot be avoided due to the spacing between the outer cylinder and the piston. The malfunctions due to stopping were significantly reduced by the applied adjustments. After many injections, 35 to 45 or more, the motor sometimes still gets stopped by powder accumulated inside the injection gun. This high

number of injections points to another problem. As mentioned before the end position of the bar changes slightly adding up after many injections and gets enhanced by the accumulating powder. This induces a shift of the bar position of a quarter rotation after 10 to 20 revolutions. 25 injections are possible before any problems occur by the bar not releasing the trigger due to the shift of the end position to a position before releasing the trigger.

The spring and the built up energy in it define the injection. By increasing the strength of the spring, the injection properties like the injection velocity can be changed. During the initial test this was done by inserting two identical springs, but the frequency of malfunctions was higher and not applicable for injections in AUG. This could be solved in the future by the use of a stronger motor or further optimisation of the injector.

5.3 Particles

The W powder used for the experiments is from Treibacher Industrie A.G. Type L29864 W100. A digital microscope (Keyence VHX-5000) was used to characterise the size and shape. The digital microscope and the optics allow to take pictures with magnifications ranging from 50 up to 2500. The device has a panorama mode that automatically takes multiple pictures in a defined area and stitches them together for pictures with higher resolution.

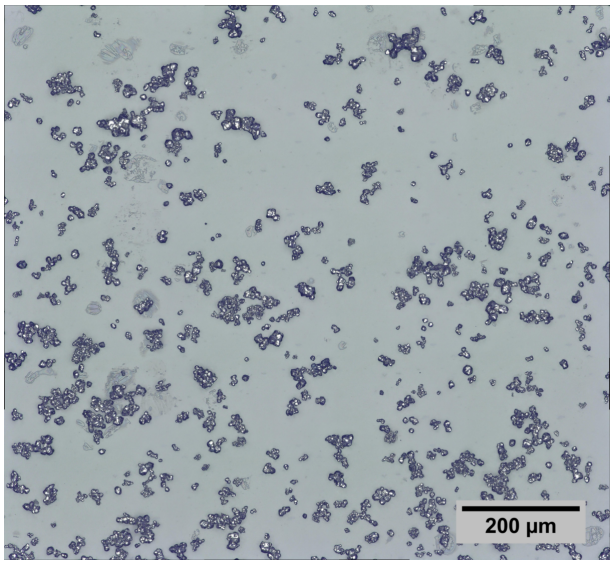

FIGURE 5.2: The picture depicts a large area of the sample with the dust. Observable are the different sizes of the dust ranging from grains with a diameter of 10 μm to agglomerates with length of 100 μm. The size of the shown picture is 1030 μm $\times$ 942 μm and is a result of the panorama mode of the device. The W grains are supplied from Treibacher Industrie A.G.

The evaluation of the pictures shows grains of different sizes and shapes. As seen in figure 5.2 a wide variety of particles is present. The powder con-

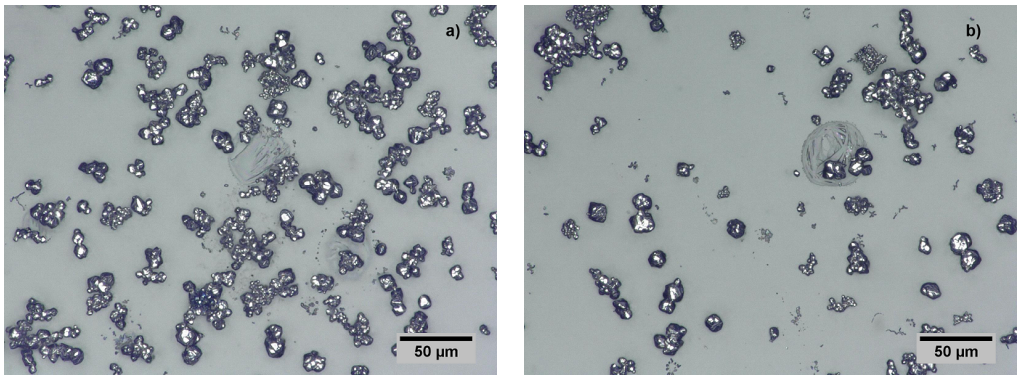

FIGURE 5.3: Both pictures show different spots with single grains, round agglomerates, stick like agglomerates and some particles with a more complicated shape. The size of the pictures is 340 μm × 255 μm. Both show the particles of Treibacher Industrie A.G.

tains many agglomerated particles that are larger than the single grains. The number of agglomerated particles is higher than that of single grains. Single grain particles are regularly observed with a size of 8 to 15 μm. These are in the most cases of spherical shape as seen in figure 5.3b shows a spot with a size of 340 μm × 255 μm.

Agglomerated particles with a size of around 30 μm are more common. Some of the agglomerated particles have an elongated shape with a width of around 15 μm which is around the size of one or two single grains. The length of these particles varies strongly from 20 to up to 150 μm in rare cases. This is observable in figure 5.2 as well as in figure 5.3a. Other agglomerates form clusters with a round shape and typical sizes of 30 to 50 μm. Large particles above 80 μm are not found frequently. Particles with a size between 15 and 60 μm are the main contribution showing different shapes from spherical to elongated.

After the first investigation of the powder and the observation of the many agglomerates the powder was placed in a small glass and put into an ultrasonic bath. The goal was to split the agglomerates into smaller grains but there was no observable, clear difference compared to the untreated particles.

This is illustrated by figure 5.4 which shows a similar size distribution as figure 5.2. A lot of agglomerates are visible as well as many small grains. Overall the difference to the untreated case is not significant and only some spots show different size distributions or less large agglomerates and more single grains. Therefore, the treatment has some influence on the sizes of the particles, but the majority does not get affected.

As a result, the powder is used without any treatment for the injection experiments and characterisation of the injection properties.

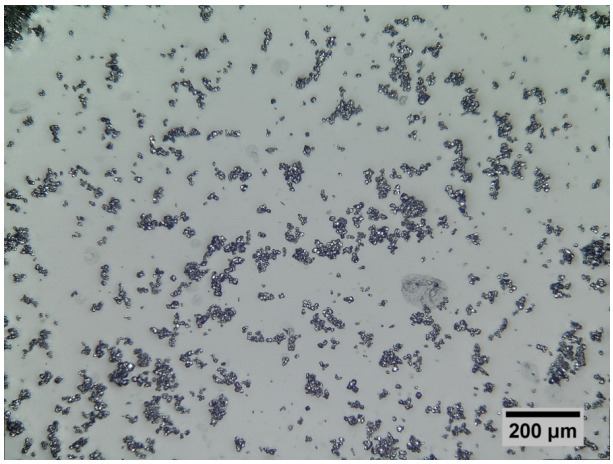

FIGURE 5.4: The picture is taken using the panorama mode. The size of the picture is $1628\,\mu$m $\times$ $1223\,\mu$m The size distribution ranges from small single grains to agglomerates with size of $50\,\mu$m. It shows the powder of Treibacher Industrie A.G. after ultrasonic treatment.

5.4 Mass

The next parameter characterised is the mass per injection. This is a important parameter for the plasma interaction because of the core W concentration limit for the AUG tokamak. The radiation of the injected particles will modify the plasma or even cause a disruption in case of the core limit concentration is exceeded. If the injected mass is significantly above the limit already a small portion entering the plasma is critical. Therefore, a reasonable injected mass is aimed for which is large enough to have an impact on the plasma but low enough not to cause a disruption. The core W limit for AUG is 1×10^{-4} of the plasma density. This is equal to around $29\,\mu$g W in the whole plasma volume for a typical discharge.

The mass per injection is also important to identify which fraction of the W dust penetrated the plasma beyond the separatrix. This portion contributes to an increase of the W concentration only. Knowing the injected mass and the core W concentration increase a penetration probability can be calculated. The mass corresponding to the core W increase divided by the injected mass gives the penetration probability of the injected powder.

During this mass characterisation additional substances like boron nitride (BN) and spherical W particles were used aside from the powder shown before.

5.4.1 Measurement method

The direct measurement of the injected mass is difficult and an indirect way to measure the injected mass is chosen. A rubber cap is used to catch the powder thrown out by one injection. The dust gets deposited inside the rubber cap and all ejected dust is collected. The net mass is evaluated by weighing the empty

cap before the injection and the filled one after the injection. The weighing machine MC 21 S from Sartorius is used to weigh the caps. The measuring error of the device is 2 μg and the readout error is 1 μg.

The following procedure is applied to determine the mass of the caps. Three balance weights from the lab are used for referencing. First, three metal weights (1 g, 200 mg and 100 mg) are weighed. Then all rubber caps are weighed. Between measurements of the different samples and reference weights it is made sure that the weighing device resets to zero when the sample is removed. This was done five times resulting in five data sets per rubber cap and balance weight. The mass is determined by calculating the difference of empty and filled caps.

5.4.2 Weight evaluation process

First for each weight or cap the average and the standard deviation are calculated from the series of five measurements. The standard deviation of the five measurements is larger than the error of the device. The deviation of each measured mass is in the order of 5 to 15 μg for W injections. In the case of W injection this is small against the calculated mass of several 100 μg. A typical W grain with a diameter of 25 μm has a mass of 0.16 μg. Hence, the deviations do not arise from one grain more or less supplied to the piston but from strongly varying particle numbers. For BN injections the standard deviation of the five measurements is in the range of 3 to 7 μg with the measured mass being several 10 μg.

The measurement of the metal weights was utilized to determine weight differences due to changed environment conditions in the laboratory. By comparing the measurements of the balance weights done together with the series of empty caps and the filled caps a weight loss or gain of them can be determined. This mass change of the balance weights is added or subtracted from the calculated weight of the filled caps. The weight loss or gain was typically small compared to the standard deviation and has minor impact on the injection mass. The deviation was of the order of the standard deviation of the balance weights at 1 to 4 μg. After taking this into account the difference of the empty and filled caps is formed to obtain the actual injected mass.

5.4.3 Injection mass

The first mass investigated corresponds to injections using the W powder described before. Later the mass of injections using (BN) and spherical W particles are investigated. As mentioned earlier two injectors were available and used for these measurements.

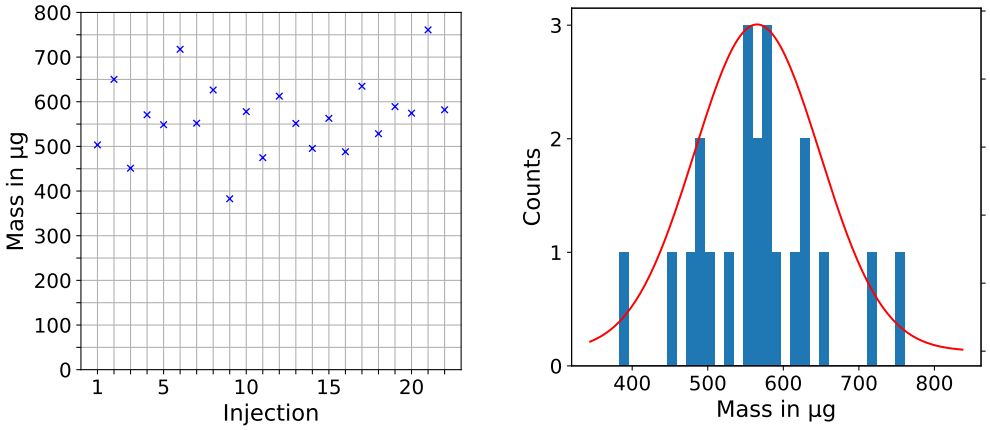

FIGURE 5.5: The mass injection per shot of two measurements series consisting of 11 caps each. Injector A is used for these measurements. The dust used is the powder from Treibacher Indistrie A.G.

5.4.3.1 Injector A: irregular W powder

Figure 5.5 shows the mass injection of Injector A of the powder from Treibacher Industrie A.G shown earlier. The 22 data points are obtained from two measurements series with 11 consecutive injections each.

As seen in figure 5.5 the measured masses are quite close together. The first 11 measurements have an average mass per injection of 556 μg with a standard deviation of 89 μg. The second set of 11 measurements has an average of 577 μg and a standard deviation of 74 μg. The observed scatter of the masses shows that the mass per shot is not constant with the same running properties but overall the masses are consistent showing not many strongly differing masses. The differences of the masses arise from the loading mechanism that is relying on the powder falling through the holes which is only driven by gravity as well as the capability of the powder to flow through the holes. The average of both measured series is 565 μg. The standard deviation of the injected mass is 83 μg which corresponds to 15 % of the mean value. Plotting both measurement series in a histogram and comparing them to the corresponding gauss fit shows good agreement and only few masses strongly deviating from the mean value.

The standard deviation of each measurement is of the order of 6 to 15 μg which is around 3 % of the mean injected mass. It is smaller than the standard deviation of the whole series. This supports the assumption that the loading mechanism is the defining source for the scattering of the masses. The errors by the measurement are significantly lower than the observed scatter of the masses and the only remaining factor is the mechanic and loading itself.

5.4.3.2 Injector B: irregular W powder

Those measurements were also done with Injector B that has a slightly different piston diameter and hole sizes to supply the powder. The results of these measurements are shown in figure 5.6. The series contains 10 consecutive shots.

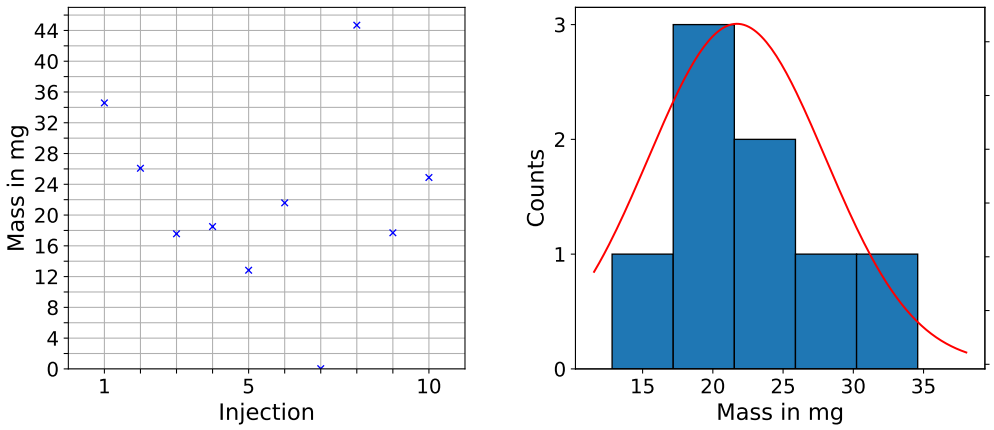

FIGURE 5.6: The mass injection per shot of one measurement series with Injector B. At injection 7 the bar got stuck after loading and no injection was performed. The next injection therefore shows a higher mass ejection. For the plot on the right point 7 and 8 are not included. The dust used is the dust from Treibacher Industrie A.G.

The injected mass is significantly larger due to the different hole diameters of this injector compared to Injector A used before. Additionally, the scattering of the masses is larger than for Injector A.

Two measured masses deviate strongly from the mean value of the other masses due to a malfunction of the injector. Those points are the masses 7 and 8 and are taken out of the calculation. They result from the bar getting stuck on the trigger after loading the powder for injection 7. As it was not sure whether powder fell into the cap it was not used again but measured afterwards. This showed that some powder had fallen out of the cylinder when pulling the piston back. For the next injection the motor was rotated back so the bar was in front of the trigger. The mass is therefore higher as powder got loaded twice. The mass of this shot does agree quite well with the double of the average of the other masses. This case shows that an optimisation of the device is necessary to get a reliable working. In the laboratory such an error can be seen and solved but for the experiment the protection cap is mounted, and the position of the bar cannot be seen or accurately adjusted.

The average mass of these 8 measurements is 21.7 mg with a standard deviation of 6.3 mg. The standard deviation is 29 % of the average injected mass. Two data points are outside the standard deviation of the mean value showing a larger scattering of the injected masses compared to Injector A.

Moreover, by comparing to the gauss fit in figure 5.6 for the mean value and standard deviation it can be seen that Injector B has a larger scattering of the masses compared to Injector A.

The mass is a factor of 40 higher than that of Injector A.

5.4.3.3 Injector A and B: BN powder

Additional tests were performed with other powders. One of the tested substances was BN. The density of BN is much lower than that of W at only $2.2\,\mathrm{g\,cm^{-3}}$ compared to $19.3\,\mathrm{g\,cm^{-3}}$ for W. Therefore, a smaller mass per injection is expected.

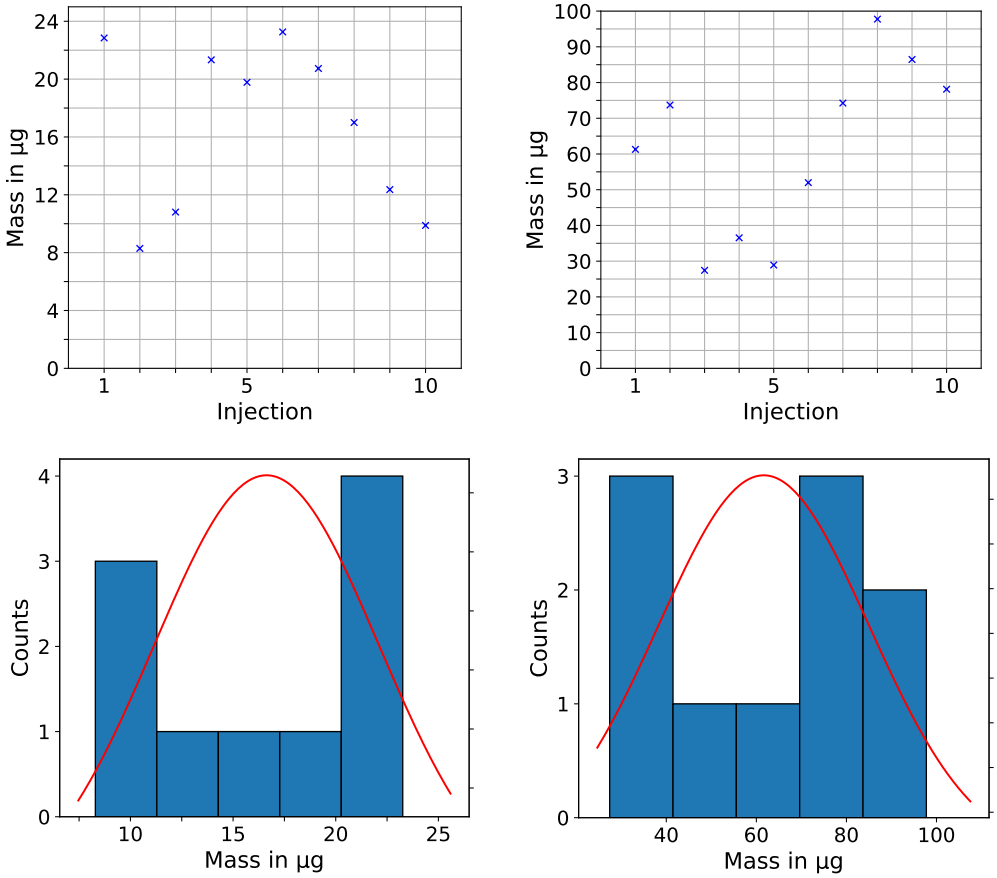

FIGURE 5.7: Results of the mass measurement using BN. The plots on the left show the mass for Injector A and the right plots belong to Injector B.

As shown in figure 5.7 the mass per injection is significantly lower than that of W. Injector A had a W mass ejection of 565 μg whilst Injector B had masses around 22 mg. The BN masses ejected are in the low 10 μg range. This applies for both injectors.

Injector A has a mean ejected BN mass of 16.6 μg. The deviation of the measured masses is 5.5 μg which is 33 % of the mean injected mass. In this

case the deviation of the mean value is of the order of the standard deviation of the single masses. This shows a higher uncertainty compared to the W measurements due to the low mass. Furthermore, the masses plotted in a histogram show a wide scatter and no mass range that occurs frequently. The masses are oriented towards the high and low end of the measured masses.

The mass injected by Injector B is at $61.6 \pm 23.4\,\mu$g. The measuring error of each mass is about a factor 3 smaller than the deviation of the different measured samples. This deviation is 38 % of the mean mass. The masses are almost homogeneously distributed over the range from the lowest to the highest mass. Multiple data points are outside the standard deviation even including the error each measured mass. This indicates the impact of the loading mechanism on the ejected mass as well as the influence of the powder used.

The stronger deviations of the masses of over 40 % of the mean value of a series could be due to the worse supply of the powder to the piston. As the powder is lighter there is less gravitational force on the powder to fall through the holes. Further, due to the shape of the powder some of it could get stuck in the hole of the magazine hindering the powder from the magazine to fall into the cavity, so it can get injected. This shows some limitations to the powder that can be injected as well as the masses of a substance achievable. Additionally, the results highlight the influence of the loading mechanism on the mass.

5.4.3.4 Injector A: spherical W powder

As seen before the used W particles have an irregular shape. An additional test with spherical and equal sized W particles was done. The powder is from LPW Technologiy Ltd. The size of the spheroids is around $30\,\mu$m. Even before the measurement of this powder it was noticed that this powder is flowing better than the W powder used before. This might lead to an increased mass compared to the irregular W powder that does not flow that well. This test was only performed with Injector A which is used for all following investigations about the injection properties.

The ejected mass per shot was evaluated in two measurement series. The first one resulted in 11 measurements and the second one in 13 masses. The evaluation of the first 11 caps filled with powder resulted in a mass per shot of 21.7 ± 3.4 mg. The second series of 13 measurements shows a mean mass per shot of 23.2 ± 3.7 mg. The deviations of 16 % from the respective mean value are similar to that of the measurement of the irregular W powder injected with the same injector. The mean value of all 24 masses is 22.5 ± 3.6 mg, which is a deviation of 16 %. The amount of W is comparable to the injections done with Injector B using the irregularly shaped W powder suggesting that the ejected mass with injector B would be even higher. The increase of the mass can be explained by the better flowing of the powder that results in a more homogeneous loading compared to the irregularly shaped W powder. The

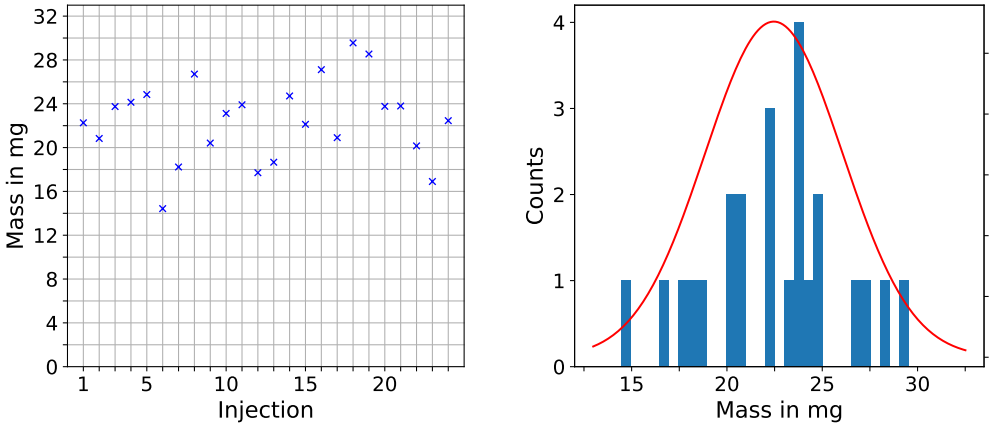

FIGURE 5.8: The injection masses of 24 measurements with the spherical W powder done with Injector A. The measurement is done in two series containing 11 and 13 caps.

spherical powder might not lead to powder getting stuck or blocking the hole of the magazine which leads to a higher amount of W supplied.

As seen in figure 5.8 the distribution of the masses does fit very well to the gauss fit for the determined mean value and standard deviation. As the relative deviation from the mean value is similar to that of the other W powder this also supports the assumption that the deviation originates from the loading process itself.

5.4.3.5 Injection mass and core W limit

Table 5.1 summarises the results of the measurements of the injection mass for the different powders tested and the two applied injectors.

	Injector A		Injector B	
powder/mass	mean	σ	mean	σ
irregular W	565 μg	83 μg	21.7 mg	6.3 mg
BN	16.6 μg	5.5 μg	61.6 μg	23.4 μg
spherical W	22.5 mg	3.6 mg	not measured	

TABLE 5.1: Results of the mass per injection characterisation of Injector A and Injector B. Values are given as the mean value with the standard deviation of the measurement series.

Coming back to the initially mentioned core W limit, one can calculate the concentration of the injected W for the plasma volume. The mean injected mass is 565 μg. The W mass equals to 1.85×10^{18} W atoms. The volume of the plasma is 14 m^{-3}. The concentration would then be 1.3×10^{17} m^{-3}. This

is 2×10^{-3} of a typical plasma density of $7 \times 10^{19}\,\mathrm{m}^{-3}$ and would be a factor 20 higher than the W core limit itself.

The penetration probability for paticles created by laser blow-off is 10 % which is equal to a screening factor of 10 [42, 43]. For the injection of the powder the probability is expected to be lower due to the lower velocity of the particles. This makes it reasonable to use Injector A for injections. For Injector B with a mass of 22 mg the number of atoms is factor of 40 higher. This would require a lower penetration probability, compared to that of laser blow-off or Injector A, to not exceed the core limit. This amount of dust is operationally not reasonable due to the large amount of W dust deposited inside the machine and the high probability to cause a disruption.

Therefore, Injector A is chosen for further characterisation.

5.5 Video evaluation

The next important quantities considered and evaluated are the initial injection velocity, the resulting trajectory of the particles and the spread of the powder cloud. These parameters are defining the main characteristics and are key parameters of the injection. They are directly linked to the spring in the injector as it is the force behind the injection and the resulting velocity of the piston.

To evaluate the initial velocity and the trajectory the same method is used. With the velocity of the dust cloud and the trajectory the range and height loss can be evaluated and characterised. Knowing the size and shape of the dust cloud after injection the necessary information about the portion of the dust reaching the separatrix can be estimated. These characteristics later on provide the data for a precise simulation of the transport and penetration into the plasma. The detailed data about the injection give very defined initial parameters for simulation and modelling.

In the following the position tracking is described. Afterwards the results of the characterisations for the different cases of an injection in air in the laboratory, in air in the vacuum chamber and under vacuum conditions in the vacuum chamber are presented.

5.5.1 Evaluation and position tracking method

To evaluate the trajectory and velocity the video data is analysed applying a global threshold to each frame of a recording. Those pixels with a signal of the laser light diffracted by the dust are obtained. Filtering the relevant pixels above a threshold allows to process the data of the position and calculate the trajectory and the velocity of the powder. The threshold is chosen after identifying signal intensities corresponding to the background by plotting the signal intensities in a histogram. The background fills most of the picture as seen in figure 4.3d or 5.11. The counts of the corresponding intensities

are significantly higher than for the intensities of the dust. The signal of the particles are those pixels with intensities distinct above the background. From the position of those pixels in each frame a mean position of the dust cloud is calculated.

Additionally, to this method a second approach to access the position of the dust is applied. For this method not all pixels of one frame above the threshold are used to calculate the mean position but only the most forward ones. The centre of the 25 most forward pixels in injection direction is calculated. This corresponds to the position of the dust cloud front.

By calculating two positions and the according velocities a comparison of the mean and the front motion can be made. As seen in figure 5.9 the different methods do not show a significant deviation for the fit of the trajectory. Only in the beginning the deviation is larger than for the rest of the trajectory. With time the recorded intensity of some cloud parts decreases so that the overall number of pixels above the threshold decreases. The number of pixels with intensities above the threshold gets closer and finally below the value chosen for the definition of the front. Then the position for both methods becomes the same.

The trajectory fit is similar and the difference at the beginning has a small influence on the trajectory fit towards the end for the method using the mean of all pixels above the threshold. The difference mainly originates from the different position of the early frames compared to tracking the front part of the dust cloud. The front tracking method is closer to the observed trajectory and to the position where the front part actually leaves the picture. In the following the front tracking method is applied for the determination of the position.

The fitted trajectory and others investigated rise in the beginning due to the powder cloud spreading and the tracking method. The upper part is brighter and at the front of the dust cloud shifting the traced front position above the middle of the injector. This increase of the dust position does not surpass the upper edge of the cavity drilled into the front of the piston. Then the dust falls down which is fitted by a quadratic function as expected for a free falling motion.

5.5.2 Evaluation issues

There are some issues occurring while analysing the videos. Some injections show a very low diffraction signal in the later frames of the recording making it difficult to identify the dust against the background. The signal intensity drops early below the limit in these frames and no data in regions far from the injector is obtained. This leads to less data points for the powder position. Those missing points can be interpolated using the trajectory fit of the obtained points of earlier frames, but few points lead to a less constrained fit for the region far from the injector. Recordings with good and long visible dust are chosen for the tracking of the dust position.

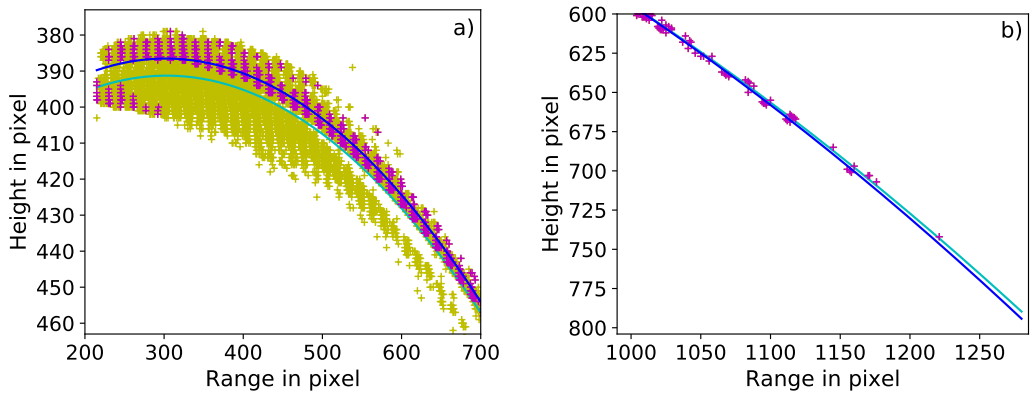

FIGURE 5.9: The plots show the difference of the tracking methods close to the injector in (a) and towards the end of the observed image section in (b). The trajectories shown in the picture are found by fitting a quadratic function to the positions found by tracking the dust with the respective method. The picture shows the dust signal for each frame superimposed. The yellow points are obtained by plotting all points above the set threshold and the cyan fitted trajectory is the respective fit to the mean position of each frame. The blue fit and the magenta points are obtained from the front method only using the 25 most forward pixels. The method considering all points is lower in the beginning as also particles of the lower cloud part contribute. Later both methods contain the same points when the overall number is below the criterion for the front. Due to the initial difference the trajectories also vary at the end. The threshold chosen for both methods is the same. The distances on the axes are given in pixels and can be converted by multiplying by $0.198\,\mathrm{mm\,px^{-1}}$. Larger versions of the pictures can be found in figure A.1 in the Appendix.

Different recordings show different ratios of dust signal to background and overall dust signal intensity. As a result of different dust intensities, the threshold to identify the dust is not the same for all recordings and varies for different recordings and injections. The limit is chosen for each injection individually but is often the same. Deviations occur as the change of the threshold is connected with different pixels contributing to the position calculation. This induces a shift of the calculated mean front position of the considered pixels and the fitted trajectory.

As seen in figure 5.10b a higher threshold in the case of the investigated recording leads to the trajectory fit being lower than for the lower limit. Other recordings can have a trajectory located higher for a higher threshold compared to a trajectory obtained with a lower limit. This leads to deviations connected with the choice of the threshold depending on the injection.

After analysing 18 injections the deviation of trajectories due to different limits is found to be in the millimetre regime. The largest separation of the trajectories induced by the different thresholds is below 15 pixels at the same

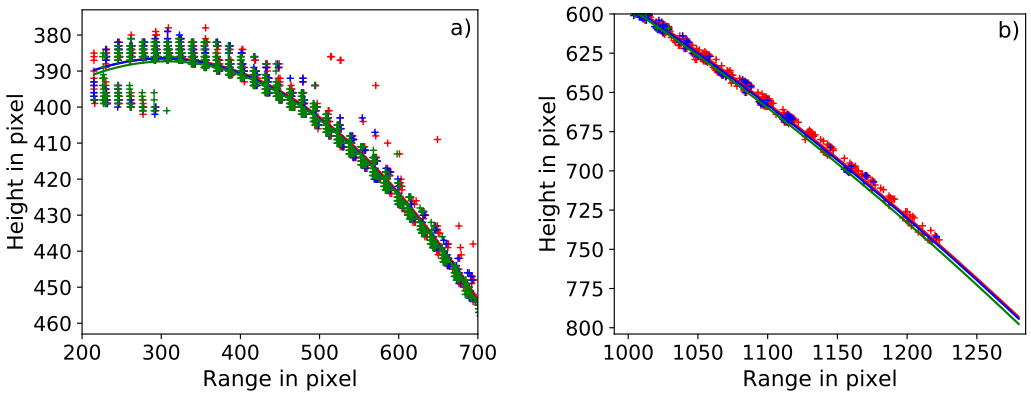

FIGURE 5.10: The trajectories shown in the pictures are found by fitting a quadratic function to the points found by tracking the 25 most forward pixels above the intensity threshold chosen for the dust. The middle, blue trajectory is obtained by applying a threshold. The red one above has a lower threshold and the green one below has a higher threshold. Points and fits of the same colour belong to each other. The difference of the higher and lower threshold from the middle one is the same. The injection analysed was an injection in the chamber under vacuum conditions. Shown in (a) is a zoom on the region close to the injector and (b) is a zoom in on the last part of the trajectory. The distances on the axes are given in pixels and can be converted by multiplying by $0.198\,\mathrm{mm\,px^{-1}}$. Larger versions of the pictures can be found in figure A.2 in the Appendix.

height or distance. This corresponds to less than 3 mm. Directly after the injection the difference is below 1 mm. At a range of 20 cm a difference of the range of below 2.5 mm is induced by a different limit. It will be shown later that the cloud is larger far from the injector than shortly after the injection and that the above mentioned deviation is smaller than the cloud extension. This shift due to the limit choice is negligible and the trajectories of different shots vary more than these aberrations which is shown later. The same applies for the error of the length calibration which is of the same order.

5.5.3 Length calibration

In order to convert the obtained pixel positions and distances into distances in units of mm a conversion factor is necessary. When recording the injection, the front part of the injector is also visible. With laser illumination the size of the cylinder cannot be defined well. An additional recording is made with illumination by a lamp which provides a better picture. This is done without changing anything of the setup to have the same setting as during the recording. The picture taken with the bright illumination can be seen in figure 5.11 allowing a precise determination of the top and bottom borders and thus the extension of the cylinder in pixel. This picture shows the field of view recorded

for the following characterisation.

FIGURE 5.11: Picture of the injector mounted in the vacuum chamber recorded for the size calibration. The illumination is done by a halogen lamp in the vessel. The resolution of the picture is 1280 px × 800 px.

From the size of the cylinder in pixels and the known diameter of the cylinder this factor can be derived. The extension is 48 px in the recording and the diameter of the observable cylinder is 9.5 mm. The conversion factor calculated is 0.1979 mm px^{-1} or 5.0526 px mm^{-1}. With this method the size of the recording, distances and objects therein can be converted from pixel into millimetre.

The size of this image is 1280 px × 800 px which converts to a size of 25.3 cm × 15.8 cm.

The error of the conversion factor resulting from a wrong determination of the extension in pixel is 0.004 mm px^{-1} for a wrong determination by 1 pixel.

The error of the calibration factor connected to an measurement error of the diameter of the cylinder of 0.1 mm induces an error of 0.002 mm px^{-1}.

5.6 Injection in air in the laboratory

As first case the injections performed in the laboratory with atmospheric conditions are evaluated. The lighting is done with the line laser. The properties of the injection investigated are the trajectory, the velocity evolution and the spread of the cloud after injection.

5.6.1 Trajectory

Outside the vacuum chamber observation is possible for long times as the camera can be placed close to the injection plane, but this restricts the observable field of view. From the evaluable time interval a trajectory can be derived.

On the other hand, this trajectory applies for the dust in the laser plane at the front only due to tracking the bright front only. The dust cloud does not have a compact shape, but some parts spread strongly as visible in figure 5.12.

This leads to only a small portion of the dust following this trajectory and a large portion of the dust spreading below and behind the tracked front. Some of the dust is not observed because it is in front or behind the laser plane from the point of view of the camera as discussed for the illumination of the dust. This makes the trajectory inaccurate as for later times only a small part of the powder follows a trajectory. A more detailed study of the shape evolution of the dust cloud after injection is given later.

Rarely a large portion of the dust stays compact in air long times to have a sufficient amount of dust that can be traced. Such an injection with a compact front is shown in figure 5.12 with the corresponding trajectory of the front. The injection was performed in the laboratory using laser illumination. The dust position was tracked up to a distance of 9 cm where the powder cloud leaves the field of view.

The trajectory is obtained by fitting a quadratic function to the obtained position data. The resulting equation of the trajectory is $y(x) = a \cdot x^2 + b \cdot x + c$. The coefficients of the equation are with their respective standard deviation $a = 3.74 \pm 0.39 \times 10^{-3}\,\mathrm{mm}^{-1}$, $b = -1.51 \pm 0.38 \times 10^{-1}$ and $c = 1.08 \pm 0.55\,\mathrm{mm}$. Six analysed injections showing a compact front lead to these values. The value of x is handed in mm to receive the height loss in mm. The direction of the y-axis is inverted compared to figure 5.12.

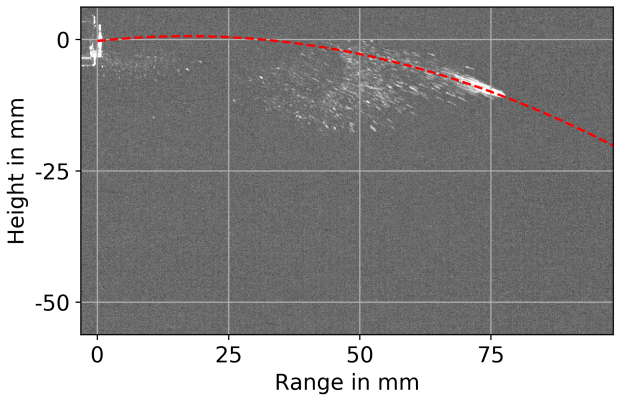

FIGURE 5.12: Trajectory fitted for an injection at atmospheric pressure. The dust cloud (white) is taken 60 ms after injection. The recording is done outside the vessel with the line laser as illumination.

As mentioned, only in some cases such a compact dust front was observed. In most other cases a huge dust cloud developed after injection with only a minor portion of it following a trajectory. This is shown in figure 5.14. Only in those injections with a compact part at the front distances in the range of 9 cm are reached. As can be seen the dust has dropped by 20 mm when leaving the field of view but this resembles only the front part of the injected dust. In air the majority does not reach the necessary distance of 10 cm.

5.6.2 Velocity

Following the investigation of the trajectory the positions determined for the trajectory in figure 5.12 are now used to calculate the initial velocity.

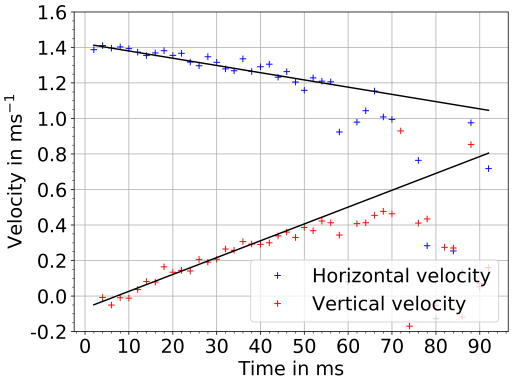

FIGURE 5.13: The velocity evolution depicted is obtained from the recording of the dust cloud in laboratory using laser illumination. For the fit of the velocities the first 25 points are used. This corresponds to an interval up to 50 ms after injection.

Figure 5.13 depicts the evolution of the dust velocity for an injection performed in the laboratory. The illumination was done with the laser.

The initial velocity of this shot is $1.4\,\mathrm{m\,s^{-1}}$. The velocity decreases right after the injection. This is expected for the injection in air as friction slows down the dust.

After 50 ms the velocity of the particles at the front has decreased by 15 % of the initial velocity. Particles behind the front get slowed down more and have no velocity in x direction after 60 to 70 ms any more.

The observed velocities of the injections showing a compact dust front result in a velocity of $1.38 \pm 0.03\,\mathrm{m\,s^{-1}}$. Six injections entered this calculation due to the limited number of injections showing a compact front.

5.6.3 Cloud spread

As mentioned for the tracking of the position for the trajectory fit the most forward dust is considered. So strictly the trajectory does only refer to the dust front. It represents the particles that could enter the plasma, i. e. have the highest penetration into the plasma. In the following the evolution of the shape of the dust cloud is investigated to determine how close the overall dust cloud is to the trajectory and range determined before.

The initial testing for the illumination showed that the dust widely spreads in air and the laser does not illuminate all dust. Especially the thin and faint parts behind the front of the dust cloud are not well resolved.

Figure 5.14 shows the evolution of the powder cloud in air recorded in the laboratory. The air injections show a large spread and particle loss along the horizontal injection direction. A lot of dust falls down behind the front

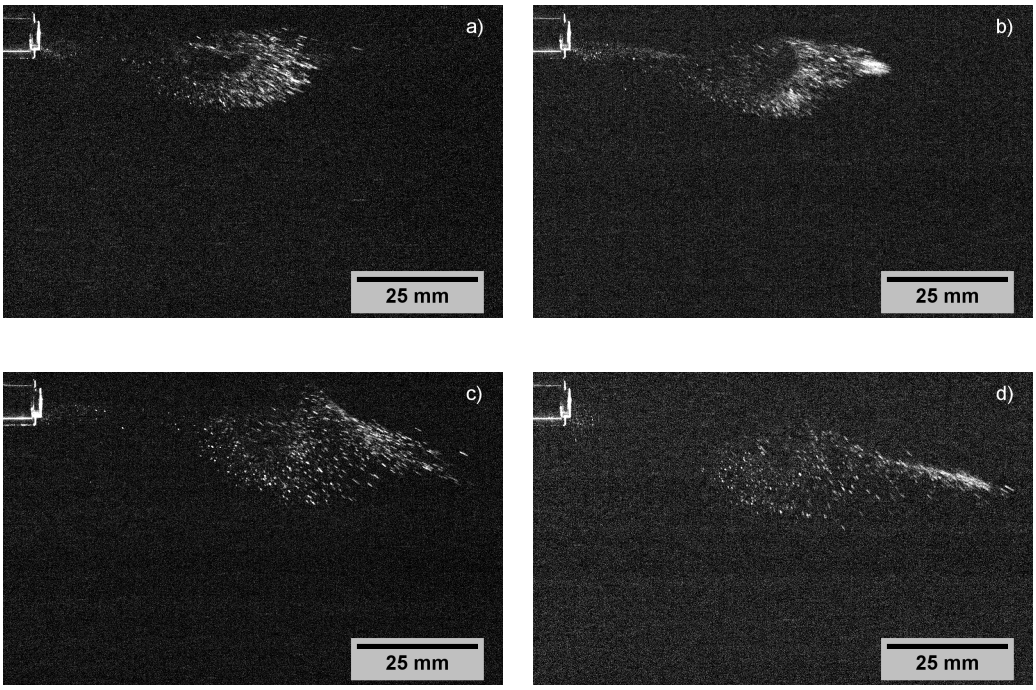

FIGURE 5.14: The pictures of different injections (a) and (b) of a cloud are taken 50 ms after the injection. The two images (c and (d show the powder cloud after 80 ms. The left (a,(c) and right (b,d) pictures illustrates the different structure of the cloud that form after injection in air. In some recordings the powder is spread over a large volume. Those shots could not be used in the previous characterisation. Other injections show a wide spread cloud but also a compact portion at the front which was tracked. All images are from recordings done with laser illumination at atmospheric pressure. The contrast has been increased to make the dust better visible. The pictures have a size of 10.1 cm × 6.3 cm.

forming a tail under the trajectory of the particle front. This is due to powder getting slowed down by the air friction and falls down by gravity. In some occasions small parts of the cloud stay compact and close together and follow a trajectory as described before. As seen in figure 5.14c injections showing no defined front part develop into a dust cloud with reduced range.

As explained with the illumination test not all dust is observed and the cloud spreads in a volume from the injector to the front horizontally and vertically. 80 ms after injection the dust cloud is spread over 10 cm horizontally and 5 cm vertically. In the case of the injection with illumination by the halogen lamp turbulent features can be seen in the powder cloud in front of the injector where the cloud is very thin. These eddies resulting from instabilities lead to a spreading of the cloud that gets amplified by these eddies. This indicates the influence of the ambient air on the cloud development. This can be observed in figure 5.15. Those recordings also show the actual size of the cloud compared to laser illumination making the front parts visible only.

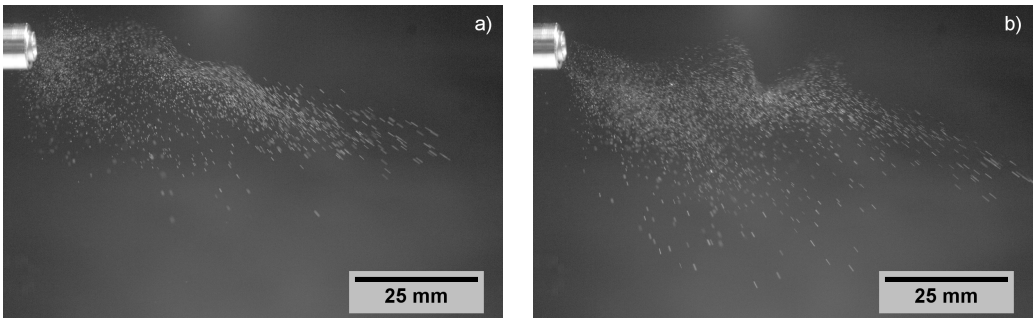

FIGURE 5.15: Development of turbulent features visible with lamp illumination in air in the laboratory. Pictures taken 74 ms (a) and 86 ms (b) after the injection. Observable is a large portion of the cloud that is not observable with laser illumination in figure 5.14. The size of the pictures is 10.1 cm × 6.3 cm

5.7 Injection in air in the vacuum chamber

Due to the installation in the vacuum vessel the distance of the camera from the dust is increased and the illumination by the laser hindered, which is also due to the increased distance from the dust. As a result, the tracking of the dust cloud in air in the chamber over a long time is difficult due to a strong spreading of the dust cloud after the injection. It turned out that under these conditions the tracing of the dust is possible for 50 ms or a distance of 7 cm inside the chamber as already discussed in chapter 4.3 and figure 4.3.

For recordings inside the vessel at atmospheric pressure no injection with a compact front with high enough intensity of the dust was observed for which a trajectory could be fitted over a reasonable distance with good agreement to the observed one. The low intensity of the recorded signal and the spread of the cloud lead to a strong scattering of the tracked position.

The size shortly after the injection inside the vacuum chamber is at around 6 mm. The cloud starts to spread and especially the lower part is affected by this and spreads faster. The cloud after 30 ms is shown in figure 5.16b. The comparison to figure 5.15 taken with different illumination shows that the faint and thin cloud locations forming behind the front parts are not visible when illuminated by the laser. 50 ms after the injection the powder cloud is widespread. The size of the visible cloud has a horizontal elongation about 25 mm and a vertical one of 20 mm. Compared to the injection in the laboratory with laser illumination the observation range and time are significantly reduced.

The evaluation outside the chamber showed that the size is much larger than the size derived from the recordings in the vacuum chamber in air. This is due to the fact that the illumination in the laboratory is brighter, uncovering even very thin regions of the dust cloud and single grains. Further to notice are the different intensities using the laser illumination in the laboratory and inside the vacuum chamber due to the distance from the injector which is

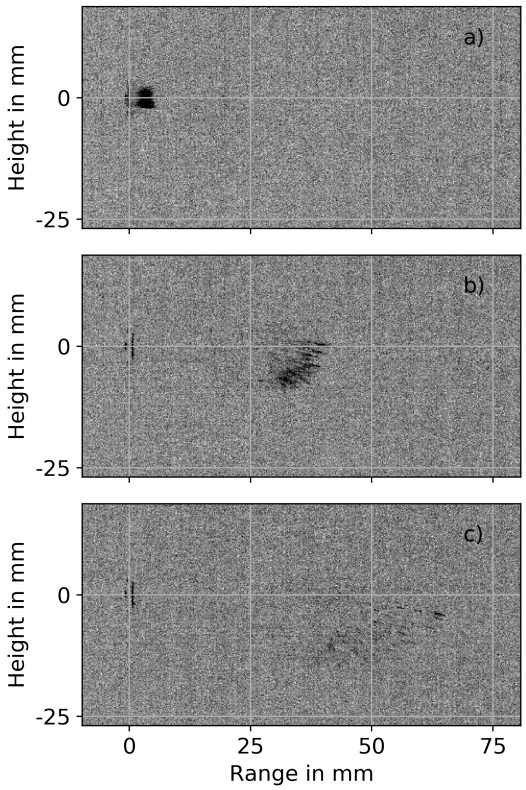

FIGURE 5.16: The figure depicts the evolution of the powder cloud inside the vacuum chamber with atmospheric pressure illuminated by the laser. Pictures taken after the injection when the cloud is fully visible (a), after 30 ms (b) and 50 ms (c). The decreasing visibility is connected to a spread of the dust. Due to the spread the cloud is barely visible after 50 ms.

connected to different sizes of the visible cloud.

5.8 Injection in vacuum in the vacuum chamber

After the analysis of the injection in air that showed a large spread of the dust after injection and that the necessary range was not reliably reached the injections were investigated under vacuum conditions.

5.8.1 Trajectory

Performing the injection in vacuum lead to a more compact dust cloud resulting in a much better determination of the trajectory similar to the case in the laboratory in air. This is the relevant case for the characterisation of the injector as it shows how the powder cloud evolves without external influences except gravity.

For the vacuum case the powder can be seen clearly, and the determination of the dust position is possible for long times. The trajectory or range for different shots is traceable up to 20 cm and the drop up to a height loss of 7.5 cm. This is limited by the field of view of the recording.

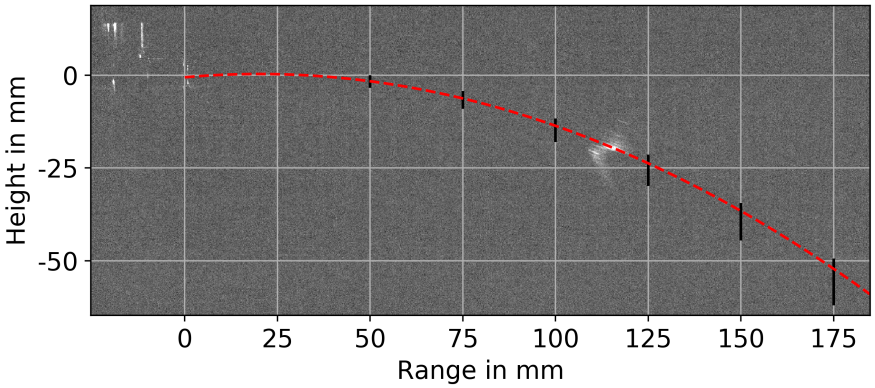

FIGURE 5.17: The fitted trajectory of an injection is shown as the red dashed line. The picture of the powder (white) is taken 80 ms after the injection. From 5 cm on the black bars indicate the drop of trajectories of different injections. The highest and lowest point correspond to the least or highest observed drop at that range. The tracked dust positions on the first 3 cm are above the middle of the injector due to the tracking and due to the shape of the injector. This shifts the trajectory above the middle of the injector.

The trajectory of the powder is again described by the following quadratic equation $y(x) = a \cdot x^2 + b \cdot x + c$. Fitting the measurements yields the coefficient $a = 2.35 \pm 0.11 \times 10^{-3}\,\mathrm{mm}^{-1}$, $b = -9.92 \pm 2.37 \times 10^{-2}$ and $c = 0.306 \pm 0.705\,\mathrm{mm}$. The coordinate system associated is a different compared to the one in figure 5.17. The positive x-axis is in the same direction but the positive y-axis is down in falling direction of the dust. $y(x)$ provides the drop of the dust injected by the injector at a certain distance in mm. The value of x is in mm and denotes the horizontal distance from the injector. The coefficients and their standard deviation are obtained from 18 injections analysed.

The trajectory fit of a typical injection is shown in figure 5.17. The analysis of different injections lead to the vertical black bars. The top and bottom of the bars indicate the positions where the highest and lowest trajectory at that range were observed.

The fitted trajectory is above the middle of the injector up to a distance of 2.2 cm due to the powder cloud spreading and the tracking method. The upper part is brighter and at the front of the dust cloud shifting the traced front position above the middle of the injector. This increase of the dust position does not surpass the upper edge of the cavity drilled into the front of the piston. Then the dust falls down which is fitted by a quadratic function as expected for a free falling motion.

The necessary range of 10 cm is reached with a drop of less than 25 mm. This position is exceeded after 68 ms. At a range of 17.5 cm the dust has dropped by 51 mm. This shows that the injector is reliably capable of ejecting the powder much further than necessary in vacuum.

To evaluate the impact of different uncertainties a look is taken at the changes due to limit setting, length calibration and different injections. The variation of different shots is larger than the deviation due to a change of the limit as seen before. The spread that can occur due to different threshold is about 5 times smaller than the one that is observed when analysing different shots at a range of 10 cm. At larger ranges it is even smaller. The error of the calibration is also small leading to a deviation of the range of 2 mm for a range of 10 cm.

Therefore, the dominant effect leading to deviating trajectories and ranges are the injections themselves.

5.8.2 Velocity

Following the trajectory the velocity evolution is analysed. It is an important parameter along with the trajectory and the mass for the characterisation of the device. The velocity has large influence on the penetration depth of the particles into the edge plasma. The effect of different initial velocities on the penetration and the release of W will be discussed in chapter 6.

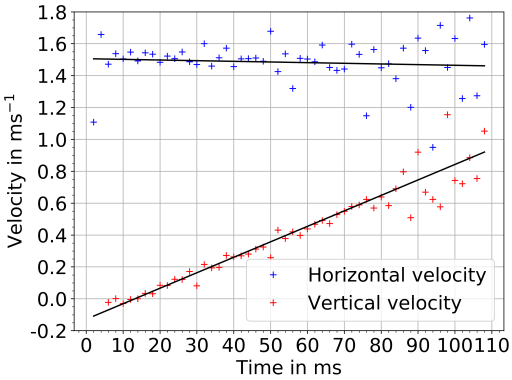

FIGURE 5.18: The velocity evolution depicted is obtained from the recording of the dust cloud under vacuum conditions in figure 5.17. To both velocity evolutions a linear fit over the first 40 velocities or 80 ms is applied.

The plot of the velocity development of an injected powder cloud in vacuum is show in figure 5.18. It is the same injection shown in figure 5.17. As under vacuum conditions friction is not present, the horizontal velocity of the dust stays constant for a long time. The velocity evolution does only show a small decrease over the interval for which the position of the dust position can be tracked and the velocity can be calculated.

The mean value over the first 40 ms after the injection is $1.507\,\mathrm{m\,s^{-1}}$ for this injection. Towards the end of this interval the velocity starts to fluctuate. This is due to the lower intensities observed which leads to an increased effect of distribution and intensity changes of the cloud itself. This makes the tracking at later times less precise than at the beginning. With time the number of tracked points decreases as shown in figure 5.9. Due to the low number of points tracked, changes of the brightest position within the cloud affects the tracked position converting into velocity changes.

The same 18 injections evaluated for the trajectory are evaluated to determine the mean velocity and its deviation. By evaluating these injections the initial velocity is found to be $1.492 \pm 0.027\,\mathrm{m\,s^{-1}}$. The velocity stays almost constant in all recordings and only decreases slightly. This is expected for the injection in vacuum apart from the decrease of the velocity, which might be an artefact of the tracking due to the spreading of the cloud and intensity changed in it.

The vertical velocity is also analysed and shows a linear increase corresponding to an acceleration of $9.64 \pm 0.51\,\mathrm{m\,s^{-2}}$. This value is around the expected gravitational acceleration of $9.81\,\mathrm{m\,s^{-2}}$, which is the only force acting on the dust in vacuum. This verifies the fitted quadratic equation and the velocity evaluation. As mentioned before only the brightest front of the dust is tracked which is always in the top section of the cloud and showing the least drop. Dust that is not visible and tracked would shift the traced position below the actual tracked dust position which would result in a higher acceleration. Overall this setup is not designed for a precise determination of the the gravitational acceleration, but this result validates the constant vertical acceleration close to the expected value which supports the quadratic trajectory fit described before. Also, by validating the vertical velocity and acceleration the obtained horizontal velocity can be assumed as accurately evaluated.

Due to the resolution of the picture and the conversion factor a tracked position of the dust that is shifted one pixel to where it is expected by a constant velocity leads to a change of the velocity of $0.1\,\mathrm{m\,s^{-1}}$. Considering this the gained velocities in the first 40 ms are in a narrow band showing only little scattering and therefore constant velocity and accurate tracing.

5.8.3 Dust cloud shape

5.8.3.1 Observed 2D size

The previous characterisation of the dust cloud backs up the idea to characterise the injection under vacuum conditions as the air environment has huge influence and impact on the development of the dust cloud after injection. In vacuum those effects should be suppressed and the characteristics of the cloud should be well observable.

The evaluation is done by evaluating the highest and lowest pixels that can be associated with the injected dust. The left and right edge of the dust cloud

which corresponds to the horizontal spread are also measured.

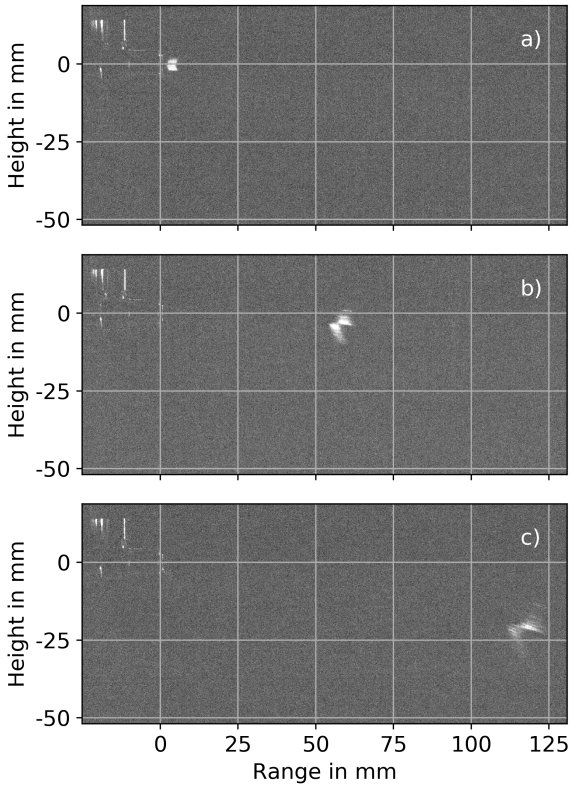

FIGURE 5.19: The development of the injected dust cloud directly (a), 40 ms (b) and 80 ms (c) after injection in the vacuum chamber at a pressure of 4.7×10^{-4} Pa. The cloud stays compact, does not spread fast and is visible over the whole distance. The shape evolution shows a consistent shape feature occurring in all recording. The illumination is done with the line laser.

As depicted in figure 5.19 the size of the cloud is clearly smaller and more compact than in air at any time after injection. The cloud evolution follows a scheme after injection and has a consistent shape. The dust cloud is clearly visible over a longer range than for injections in air in the chamber or laboratory. Also, the intensity of the light scattered by the dust only decreases little indicating only a minor loss of powder. The overall intensity indicates that the powder density of the cloud is high.

After injection the horizontal and vertical extension of the dust cloud are 4 mm and 5 mm, respectively. After a time of 40 ms as in figure 5.19b corresponding to a distance of 6 cm the extension of the cloud are 7 mm horizontally and 10 mm vertically. The dust cloud after 80 ms at a distance of 12 cm from the injector is shown in figure 5.19c. The horizontal extension is 13 mm and vertical extension is 17 mm. Due to the small but continuous spread of the dust the intensity decreases stronger in the lower part.

By evaluating the size of multiple dust clouds an average size of 10 ± 2 mm and 13 ± 2 mm is found 10 cm from the injector which is the planned distance

from the seperatrix. 20 cm from the injector the mean size is 21 ± 2 mm and 24 ± 3 mm.

In the vacuum case apart from the size of the cloud a structural feature can be identified in all recordings. The ejected powder has a distinct shape where a pronounced upper and less pronounced lower part can be observed as in figures 5.19b and 5.19c. The lower part is pointing down and forward and is quite straight. With time this structure gets longer and the intensity decreases. The upper part is pointing horizontally. This part is bulkier and sometimes almost round in the beginning, although, the horizontal length varies a bit. At later times the upper part gets thinner and longer forming a line with a small downward component. The upper part contains more dust judging from the intensity of the reflected light over the curse of the injection. The intensity of the lower part starts to decrease earlier and is barely visible at a distance of 20 cm. Even at this distance the upper part can still be recognised well indicating that the particle density is higher. The change of the lower part and the change of the upper part from compact to a elongated structure show that the cloud is prone to a spread and that there are particles with different velocities present.

The observed shape of the cloud is due to the injector and the geometry of the cavity from which the dust is injected. Injector B showed another, consistent shape of the cloud. The shape of the dust cloud is a feature of the injector. When accelerated the dust is pressed against the back of the moving cylinder. Upon injection two sections form, an upper and a lower part that separate with increasing distance from the injector. The lower part is always lower and behind the upper part. This has an effect of the range of the dust. The upper portion has a 15 to 20 mm larger range compared to the lower portion for ranges above 10 cm.

5.8.3.2 3D cloud approximation

During the analysis described above only the 2D extension of the cloud as illuminated by the laser could be accessed. The dust is only recorded parallel to its trajectory. The component parallel to the camera view cannot be resolved. In addition, only a 2D plane of the dust cloud is illuminated by the laser and no 3D information is contained in the recordings. The recordings in the laboratory with the lighting by the halogen lamps indicated that there is dust not illuminated by the laser. To interpolate this for the 3D cloud an estimate for this direction parallel to the camera view is looked for.

This extension is approximated by looking at the spread of the powder on a sheet of paper. The sheet of paper was placed 15 cm below the injector to investigate the dust impact region in air. In the range of 1.5 cm perpendicular to the injector axis the majority of the dust was deposited. As this is done in air the spread in vacuum is expected to be smaller as seen for the investigation of the cloud in air and vacuum. On the other hand comparing the height of the cloud in air in the laboratory in figure 5.14 and in vacuum in figure 5.19 they

are similar but the horizontal extension is different. It is assumed that the size is two thirds of that in vacuum. It then increases from 6 mm which is the diameter of the cavity to 15.2 mm at 10 cm and 24.6 mm at 20 cm. Therefore, the approximation seems reasonable considering that the travelled distance of the dust is larger than that of the dust observed in the recordings.

The total size of the powder cloud in vacuum is increasing from around 4, 6 and 6 mm at 5 ms after injection to about 10, 13 and 15 mm at 10 cm. At distance of 15 cm the size is 17, 20 and 25 mm. The sizes are given as width and height as observed in the recordings and the approximated size in the direction parallel to the camera.

The size in the observation plane can be determined accurately in vacuum whereas the third dimension is imprecise because of the estimation and the interpolation from the injection in air. The given size for this direction is only an estimate.

5.9 Dust range

Combining the information gained from the vacuum injections about the trajectory tracking the front of the upper part and the size evolution of the cloud the portion of the dust at different ranges can be described.

All the observed dust reaches a range of above 10 cm with different height losses as seen for different injections in figure 5.17. Taking into account the shape of the dust and the observation that the upper part is brighter than the lower part this lead to the conclusion that this cloud part has a higher particle density and therefore the majority of the dust is there.

Simulating particles with the obtained initial velocity will represent and account for the majority of the injected dust. The dust below the trajectory with a lower recorded intensity does only have a small reduction of the range and does reach the same ranges as the top part following the trajectory but with a larger height loss.

Regarding the initial conditions used for the simulation of the dust injection into plasma, this means that the major portion of the dust follows the determined trajectory with the given initial velocity. These values are used for the simulation of the dust injection into plasma.

5.10 Comparison to Korean Characterisation

The results can be set into perspective by comparing them to the characteristics that were obtained at KAIST. A short comparison to the performance of the injector in [7] is given as such a device was supplied and used for the performed characterisation.

The first difference is that the experiments of [7] were only performed under atmospheric conditions which at the present investigation did not provide useful information for the characteristics.

Further, the W material used in the tests in [7] is different. In those experiments cylindrical shaped W particles with diameters around 0.1 mm and length of 1 mm were used. Those are significantly larger than the grains and particles in the powder investigated here. The injected mass is around 15 mg which is closer to that of Injector B than the used Injector A.

According to performed injections with the injector at KSTAR tokamak [6] the particles used ranged from 10 to 100 μm and the injected mass was about 2 mg. Those particles are similar to the ones evaluated during this investigation but the mass obtained from the characterisation of Injector A is smaller hinting to differences of the injector.

As reported in the characterisation of [7] 90 % of the W particles reach a range of 10 cm. Under atmospheric conditions this was not expected due to the strong friction effect and spread of the dust. In vacuum this range was well achieved and the results were similar to the ones obtained at KAIST.

The velocity in [7] is given as 2 to 4 $\mathrm{m\,s^{-1}}$. This is higher than the velocity observed in this experiment. The range of 10 cm is given with the drop for different W particles. The drop of these grains is lower at the range of 10 cm than in the experiments described here. The differences could be due the use of a different spring.

Experiments at KSTAR [6] with such an injector showed that the injected dust has a strong influence on the plasma operation leading to disruptions shortly after the injection of the W powder. The studies focused on the transport of the injected particles. The injections were recorded with a fast camera to compare them to a particle simulation. The recordings showed two different behaviours of the dust as one portion was dominated by gravity and the other one was transported in toroidal direction by the ion drag. The first class was associated with large and heavy particle whereas the second one with small and light particles. Simulation using the observed trajectories of the dust lead to good agreement of the trajectories of the large grains with the observations of the presumably large grains. For the simulation of the small grains with the toroidal motion the trajectories of the simulation are much shorter than the observed ones, which is due to limitations of the applied code. During the injections the core W concentration was not measured, and no penetration factor could be calculated. Therefore, no information about the penetration or the increase of the core W concentration was gathered. Only the occurrence of disruptions gives a rough indication of the effect of the injected W. Differences to these results might occur due to the use of a different injector with other properties as explained above and different plasma parameters as the experiments will be done at the AUG tokamak.

5.11 Conclusion on Characterisation

During the operation in vacuum or in the tokamak the motor and the injector cannot be accessed. Therefore, the injector must operate reliable and

predictable. This was shown with the previously done characterisation.

The reliability was shown by operating the motor under different conditions, air and vacuum, making sure that the injector does carry out the needed amount of injections without a malfunction. The consistency and predictability were shown by the characterisation and the underlying uncertainties. The largest impacts are the difference of different injections and the mass deviations due to the loading mechanism.

The number of consecutive injections without failure is approximately 35. The number of injections is limited by a small position change of the motor and the attached bar with every revolution. 10 to 20 injections shift the bar position by a quarter circle against the running direction of the motor. This sets the limit of consecutive shots to 25 injections.

As seen the used powder does not consist of uniform grains but of agglomerates. There are more agglomerates than single grains. Grains have a spherical shape and a diameter of around 20 μm. The agglomerates are around 30 to 60 μm long and 10 to 20 μm wide resulting in an elongated shape.

As shown, different powders can be injected with a powder specific mass per injection. The W powder and injector were identified which provide a reasonable mass per injection, i. e. the mass is high enough to expect a noticeable increase of the core W concentration but low enough not to cause a disruption. During the characterisation a mass of 565 μg per injection was determined for Injector A. This mass is a factor 20 higher than the core W limit. Injector B as well as the spherical W powder injected by Injector A led to a much larger mass that is considered not reasonable for operation. The reason for the scattering of the masses was the loading mechanism of the powder as the measuring errors are much smaller than the standard deviation of the mean mass. The influence on the core depends on the penetration which is evaluated with a simulation.

The characterisation of the injection in air and in vacuum showed differences. The initial velocity of the dust after injection for both cases is almost equal with a decrease in air due to friction. As a result of the friction effects in air the maximum range of the cloud is decreased compared to the injections in vacuum. An exception are those injections showing a compact front which is less affected by the friction and spreading but also have a reduced range compared to the vacuum case. The reason for this difference is the different shape of the particle clouds and the friction effect of the air. In air the cloud size increases due to instabilities, visible by the turbulent structures in figure 5.15 that alter the shape of the cloud and lead to the spread of the dust. As a result, the friction effect on the dust particles increased, which leads to a further spreading of the cloud as well as stopping the forward motion of the particles. The size of the cloud the same time after the injection is very different. This is the biggest and most important difference.

The evaluation of the different properties proofs that the necessary range of the powder is achieved as seen in figures 5.17 and 5.19. The largest drop of a trajectory observed at a range of 10 cm is 18 mm. The observed dust cloud

has an extension of 10 mm in the horizontal, 13 mm in the vertical and 15 mm in the direction perpendicular to the injection plane. This validates that the majority of the powder reaches the separatrix from the installation position under vacuum conditions.

After making sure that the injector works reliable and the characteristics of the injection are known the injector was installed on the MEM. The injector was mounted on the MEM but the planned operation has been delayed due to repair and maintenance after a water/steam leak at AUG.

The mounted injector with the protection cap can be seen in figure 5.20. The injector and motor under the cap are arranged as shown in figure 3.1. The tip of the injection gun penetrating the protection cap can be observed in the lower part of the protection cap at the front. For the experiments the injector will be moved to its final position in the tokamak.

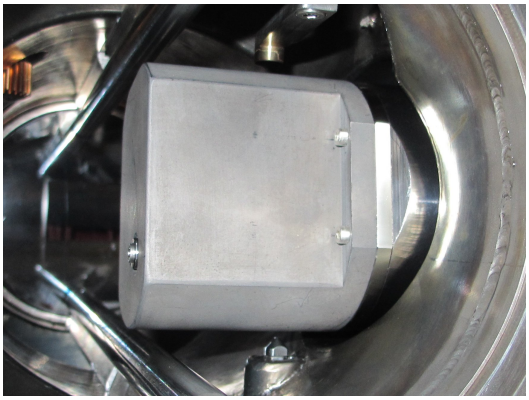

FIGURE 5.20: The injector is mounted on the MEM of AUG with the installed protection cap required for operation. In the lower part of the cap the tip of the injection gun penetrating the cap can be seen. On the right the mounting on connection to the MEM is visible which corresponds to the brown connection of base plate and MEM in silver seen in figure 3.1. This allows to adjust the position of the injector and move it into the tokamak that is on the left outside the field of view of the image.

Information about the penetration will be gained by modelling the injection by applying a simulation code for dust particle trajectories using the injection parameters of the injector.

Chapter 6

Modelling

After the characterisation of the device and before an operation in AUG the injector parameters are used to simulate the injection. Operation in AUG was planned but due to delays of the operation after a major water leakage could not be performed. The results of the simulations give an estimate of the penetration depth of different grain sizes and the locations where W is released along their trajectory. To study the influence of the initial velocity, simulations are done with different velocities.

This will also show changes of the trajectories by the plasma compared to the vacuum case of the characterisation, e. g. whether the range of the dust is decreased. Depending on differences between simulation and later experiments the code can be adjusted to reproduce the experiment. In case of good agreement of a simulation and experiment, the modelling can also be used to extrapolate future devices.

6.1 Modelling code

The DUCAD code (DUst Characterisation And Dynamics) [44], provided by Guillermo Suárez López, was used for the simulation of the dust behaviour. The code is based on the orbit limited motion (OML) theory.

The DUCAD code was developed to obtain the dust sizes of particles from fast camera recordings by comparing the simulation with the experimental trajectories [44, 14]. This was found difficult due to little effect of the simulated particles when changing their size due to the high velocity and inertia. While some features of the experimental trajectories were well reproduced by the code some aspects could not be modelled and the simulation shows deviations from the observed trajectory.

In this work the code is used to simulate the trajectory without the intention to identify the size of observed particles as it is known but to simulate the trajectories of particles to estimate the result of future experiments. Of special interest are the penetration depth and the mass release of the simulated grains.

A detailed description of the code is given in [44] and important points are presented in the following.

A basic assumption of the code is that the the particles are considered as pure W spheroids due to computational and analytical reasons. There are no wall collisions that alter the trajectory of the particles and the ablation cloud of the grain is not implemented which may alter the plasma conditions. For bigger particles and strong erosion significant local cooling of the plasma will occur, which will influence the further erosion as well as the penetration. For the simulations a constant time step is used which adds uncertainties in the region with steep gradients around the separatrix position.

The code has different routines to calculate the properties of the dust as it is moving in the plasma. This includes charging, heating and mass loss of the grain and the calculation of the forces on the grain to obtain the acceleration and position of the next time step. The terms and formulas for these calculations are inspired by other codes as DTOKS [45], DUSTT [46] and Migraine [47]. The equations in the following are taken from [44].

6.1.1 Dust charging

The charging of the dust is described by the following equation:

$$\frac{dQ_d}{dt} = \sum_Z I_i + I_e + I_{th} + I_{see} \tag{6.1}$$

In this equation Q_d is the dust grain charge $Z_0 \cdot e$. I_i and I_e are the ion current of ions with charge Z and electron current to the grain. I_{th} is the thermionic emission of the grain and I_{see} the current due to secondary electron emission. In typical SOL conditions dust charging can be assumed as an instantaneous process, which results in the relation $I_{tot} = \sum_Z I_i + I_e + I_{th} + I_{see} = 0$ that is calculated in every time step. As these currents are depending on the charge of the grain these terms are calculated for a range of charges of the grain. From the minimisation of I_{tot} the charge of the grain is obtained.

6.1.2 Dust heating

The temperature of the dust grain in DUCAD is obtained by solving the differential equation for the enthalpy:

$$\frac{d(M_d\, h_d)}{dt} = \sum_Z Q_i + Q_e + Q_{th} + Q_{see} + Q_{isn} + Q_{rad} + Q_{vap} \tag{6.2}$$

Q_i and Q_e are the heat fluxes due to ions and electrons, Q_{th} and Q_{see} are the heat fluxed connected to thermionic and secondary electron emission. Q_{isn} the heat flux due to ion surface neutralisation and Q_{rad} and Q_{vap} account for thermal radiation losses and due to atoms lost by vaporisation. This is limited

to temperatures up to 6000 K as above no enthalpy data for W is implemented due to insufficient literature sources.

6.1.3 Grain mass

The mass evolution is written as:

$$\frac{dM_d}{dt} = \frac{dM_d^{vap}}{dt} \tag{6.3}$$

The only mass loss mechanism considered in DUCAD is the vaporisation of the dust grain calculated by the Hertz-Knudsen formula. Mass loss mechanisms due to sputtering, ion implantation or backscattering of ions species of the grain material are not implemented.

6.1.4 Forces

To propagate the particles DUCAD calculates the forces acting on the grains.

$$\frac{M_d\, dv_d}{dt} = \sum F_i + F_e + F_g + F_{roc} + F_n \tag{6.4}$$

The forces calculated are the ion drag force F_i containing contributions of scattering and absorption of plasma ions, electrical forces F_e, the gravitational force F_g, the rocket force F_{roc} and the neutral friction force F_n. Magnetic field effects are marginal in this regime and are neglected for the dust dynamics.

6.1.5 Plasma background

To calculate the interaction of the dust grain with the plasma a plasma background is needed. A 3D background plasma is used due to the 3D motion of the grain. Unfortunately, only a limited set of validated plasma reconstructions are available. For the simulation of the injection of dust into plasma a plasma background calculated with the code EMC3/Eirene was used. From this DUCAD reads the data for the plasma as well as the computational grid which resembles 8 sectors. This is half of the torus. The plasma background used in the following simulations is the AUG shot # 29464 at 2500 ms when the current flat top was reached. This discharge was a deuterium plasma performed in L-mode. The plasma current was 0.8 MA. The toroidal B-field of this discharge was $B_t = -2.519\,\mathrm{T}$ and auxiliary heating was only provided by ECRH with 0.592 MW. The average electron density was $n_e = 2.16 \times 10^{19}\,\mathrm{m}^{-3}$. The safety factor at 95% of the toroidal flux is $q_{95} = 5.365$. Figures 6.1 and 6.2 show the values of the plasma parameters used for the simulation of the electron density n_e, neutral D density n_D, electron temperature T_e and ion temperature T_i.

The electron density and temperature at the height of the injector are illustrated in figure 6.3 which depicts the radial evolution of these parameters. The small gap between the red and blue part results from the transition of

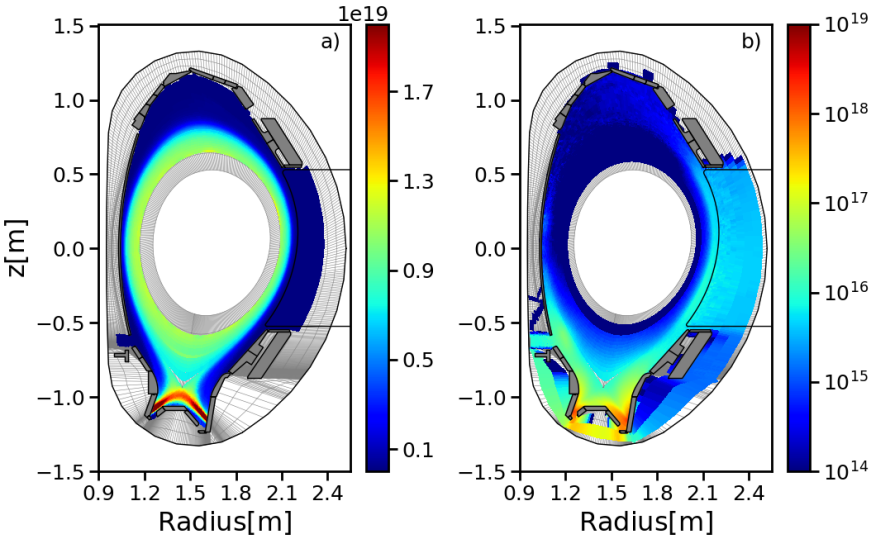

FIGURE 6.1: Plot of the poloidal cross section of the background plasma values for the electron density in m^{-3} (a) and the neutral D density in m^{-3} (b) of discharge # 29464 at 2500 ms.

computation regions. The red part corresponds to the calculation grid of the core region whereas the blue part is from the SOL region. Therefore, the change of the colours describes the location of the separatrix of the computational grid at the height of the injector.

6.2 Modelling results

The complete views of the toroidal and poloidal view can be found in figure B.1 and B.2 in the Appendix. Moreover, they contain the coordinate systems for the following plots. The close views on the trajectories in the following show the relevant sections of the plots with the simulated trajectories only.

The coordinate system of the toroidal, top view of the tokamak is a cartesian coordinate system. The x- and y-axis pass through the center of the tokamak. The ϕ coordinate gives the angular position in this plan. It is zero on the x-axis and increases in counter clockwise direction. The z coordinate is perpendicular to the plane and provides the distance to the shown equatorial plane.s

The poloidal view is a slice through the torus. The x-axis plots the R coordinate which gives the radial distance from the central axis of the torus and the y-axis plots the z coordinate that provides the height in the device. The origin of this axis is at the equatorial plane of the device.

The initial position of the simulation is the position of the injector on the MEM in the torus at $(R[m], \phi[°], z[m]) = (2.18, 168.75, 0.312)$. R is the distance from the central torus axis, z the distance from the equatorial plane

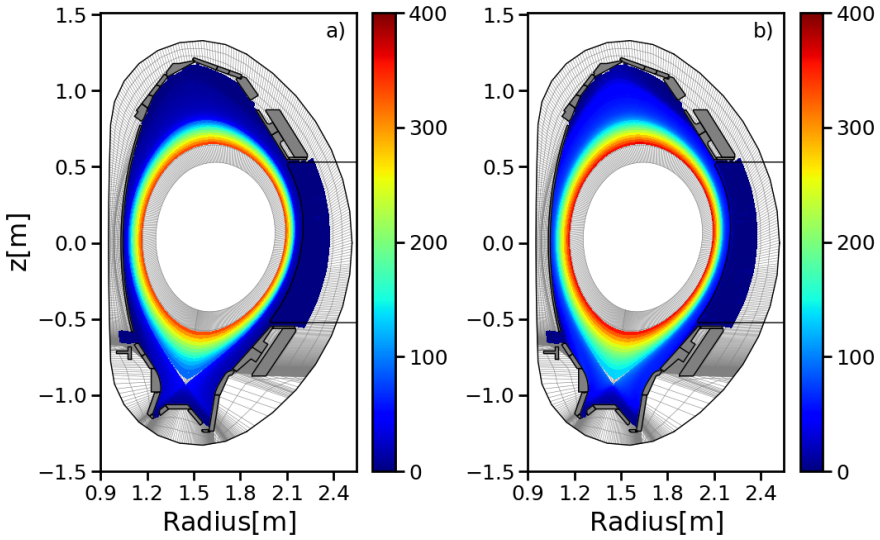

FIGURE 6.2: Plot of the background plasma values for the electron temperature in eV (a) and the ion temperature in eV (b) of discharge # 29464 at 2500 ms.

of the device and ϕ is the angular position in the toroidal view.

The initial velocity in cartesian coordinates of the toroidal view is

$$\begin{aligned} v_{ini}[m/s] &= (-1.5 \cdot cos(168.75/180 \cdot \pi), -1.5 \cdot sin(168.75/180 \cdot \pi), 0) \\ &= (1.471, -0.293, 0) \end{aligned}$$

in radial inward direction with the magnitude $1.5\,\mathrm{m\,s^{-1}}$ taken from the previous characterisation. There is no z component as the injection is horizontally.

For the modelling different grain sizes are chosen to resemble particle sizes of the dust found inside the machine [13] as well as of the powder used for injection. Calculations are done for particles with a diameter of $1\,\mu$m, $2\,\mu$m, $10\,\mu$m and $25\,\mu$m.

6.2.1 Injector modelling

For the calculations a time step of $50\,\mu$s is chosen. The simulation for each particle is run until the particle is evaporated or in a region far from the plasma.

The obtained trajectories are illustrated in a toroidal, top view in figure 6.4a and a poloidal slice in figure 6.4b. The toroidal displacement of the $1\,\mu$m and $2\,\mu$m grain is significantly larger than that of the larger grains. In the poloidal view the trajectories show a large difference for the case of a very small grain, $1\,\mu$m, and the larger grains. The $1\,\mu$m grain does get accelerated back to the wall and is in the limiter shadow after crossing the solid black line in figure 6.4b. The trajectory continues as collisions with the wall are not implemented. The $2\,\mu$m lies in between the $1\,\mu$m and the larger grains. It shows large toroidal displacement as the $1\,\mu$m grain but does not get accelerated back

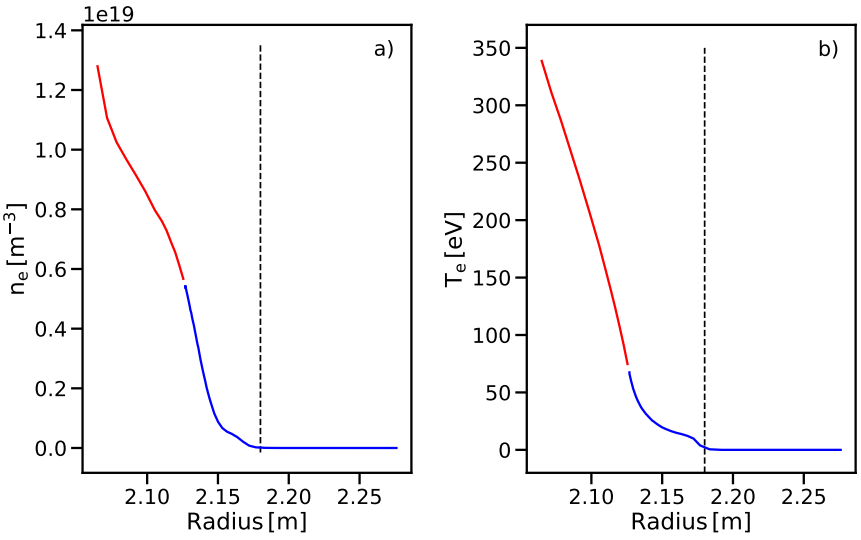

FIGURE 6.3: Electron density (a) and temperature (b) as function of the radial direction at the height of the injector. The red curve corresponds to the core region of the code and plasma reconstruction and the blue to the SOL region. The dashed vertical lines mark the position of the injector which is the initial position of the radial inward motion of the grains.

to the wall and approaches the separatrix as the larger grains. The difference of the 10 μm and 25 μm is rather small evaluating the trajectories of them. The 10 μm grain has a little larger displacement in the toroidal and poloidal direction which shows that the inertia of the grains has a dominant effect over the forces acting on them. This does not apply for the smaller grains as they are significantly influenced by the interaction with the plasma and the forces acting on them. The penetration depth is smaller than that of the 25 μm grain.

All simulated particles with the injector parameters do not reach the separatrix position except the 25 μm grain which comes close to the separatrix, enters the calculation grid of the core region and evaporates eventually. In the core region and close to the separatrix the calculated trajectory is not accurate due to limitations as no ablation cloud is considered and missing enthalpy for temperatures above 6000 K. When approaching the separatrix the gradients of T_e and n_e get steeper and lead to uncertainties due to the constant time step of the calculation. The motion deeper into the core plasma is reasonable as the grain does not get slowed down when approaching the separatrix but is accelerated.

The development of the grain radius and velocity are shown in figure 6.5. The velocity increases slowly. The 1 μm and 2 μm accelerate faster due to their lighter mass. The velocity of the 1 μm grain does not get accelerated further and stays constant when moving away from the plasma. The strong oscillations near the evaporation are a result of the increasingly steep gradients and the constant time step. Some grains show a significant velocity increases

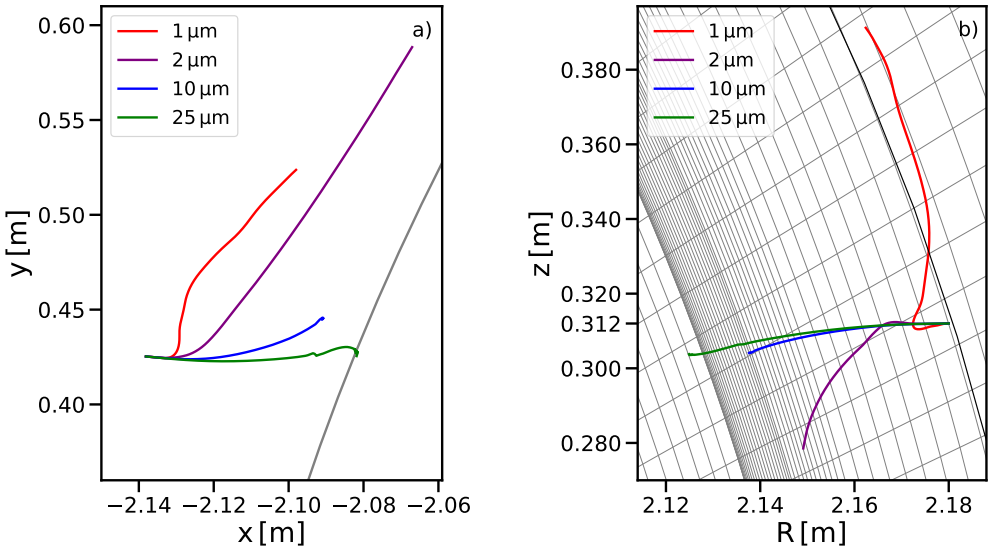

FIGURE 6.4: (a) Close view on the toroidal projection of the trajectories calculated with DUCAD. The grey line indicates the separatrix position at the height of the injector. (b) Close view on the poloidal projection of the trajectories of the DUCAD simulation in the AUG tokamak. The marking on the y-axis at 0.312 m indicates the position of the injector. The 1 μm grain in red, the 2 μm one in purple, the 10 μm in blue and the 25 μm one in green. The full toroidal view can be found in B.1 and the poloidal view in B.2.

a few ms before the grain evaporates but the results may be artefacts due to the limits of the code. For the 25 μm grain almost no change of the velocity is observed which shows the dominant effect of the inertia of the grain compared to the plasma forces acting on it. The forces responsible for the acceleration of the grains are shown in figure 6.8 for the 25 μm grain and are explained later.

The temperature evolution of the grains is illustrated in figure 6.6. For the 1 μm and 2 μm grain the temperature increases quickly whereas it rises slower for the 10 μm and 25 μm grain. This is due to the much larger mass and the larger amount of energy needed to heat the grain. The temperature of the 1 μm grain decreases after 10 ms because the particle moves away from the plasma as seen for the trajectory of the grain in figure 6.4b. For the other grains the melting of them can be observed by the temperature plateau at 3695 K. Upon reaching a temperature of 6000 K, the 10 μm and 25 μm have the maximum temperature calculated by the code. Sublimation enthalpy as well as molar enthalpy for temperatures above 6000 K are not implemented. Additional heat fluxes to the grain do not increase the grain temperature. The grains in this case evaporate in the next calculation step after reaching this temperature and the simulation stops. The grains then enter as W plasma and cannot be considered a grain any more which does not allow to give a position of the grain. Moreover, towards these temperatures the calculation

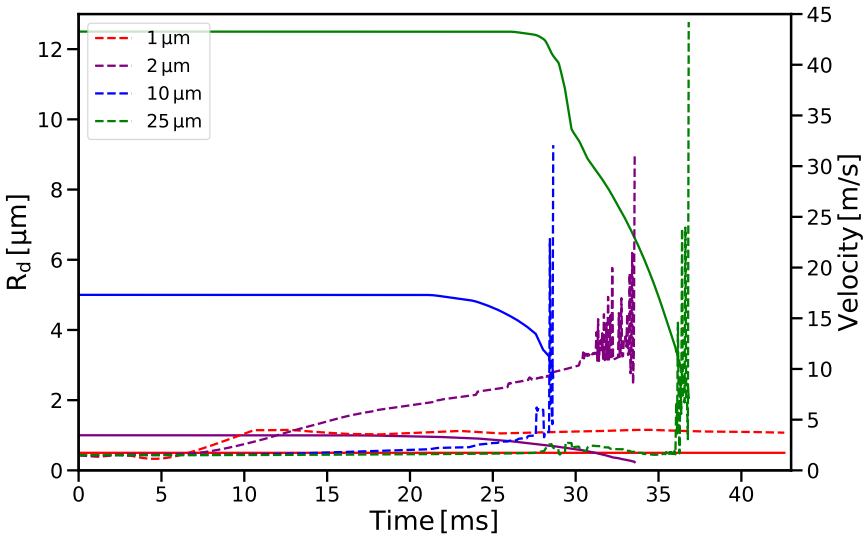

FIGURE 6.5: Development of the grain radius (solid) and the grain velocity (dashed) with time after injection. The last plotted radius of the 2 μm, 10 μm and 25 μm grain is the one before the grain is evaporated. The behaviour of the 1 μm grain is shown in red, the 2 μm one in purple, the 10 μm one in blue and the 25 μm one in green.

is not precise as no ablation cloud is considered in the code that breaks the assumption of OML theory.

The important point to evaluate the penetration is the mass loss of the grain along the trajectory. The development of the radius in time in figure 6.5 further shows that the ablation of the grain sets on when or shortly before reaching the melting temperature. The focus here is on the position of the mass release compared to the separatrix position. In terms of operation, mass release inside or close to the separatrix is more critical than the release far from it.

Therefore, the mass of the dust grain is plotted against the radial coordinate of the AUG tokamak shown in figure 6.7. The grain ablation is negligible in the beginning but significantly increases when the grains approach the separatrix. This is due to the steep temperature and density gradients around the separatrix and therefore the rising grain temperature. The reason for the low mass loss at the beginning is that the only implemented mass loss mechanism is vaporisation that requires high temperatures. These are not present at the injection position as depicted in figure 6.3. Physical sputtering as erosion mechanism is not implemented in the code. This is a valid assumption as the sputter yield for D on W is quite low.

The major mass loss of the particles is always close to radial position where the grains evaporate. The exeption is the 1 μm grain which does net experience any mass loss as it does not reach sufficiently high temperatures because it is accelerated away from the plasma towards the wall. As seen for the trajectories only one of the simulated particles reaches the separatrix. The other grains

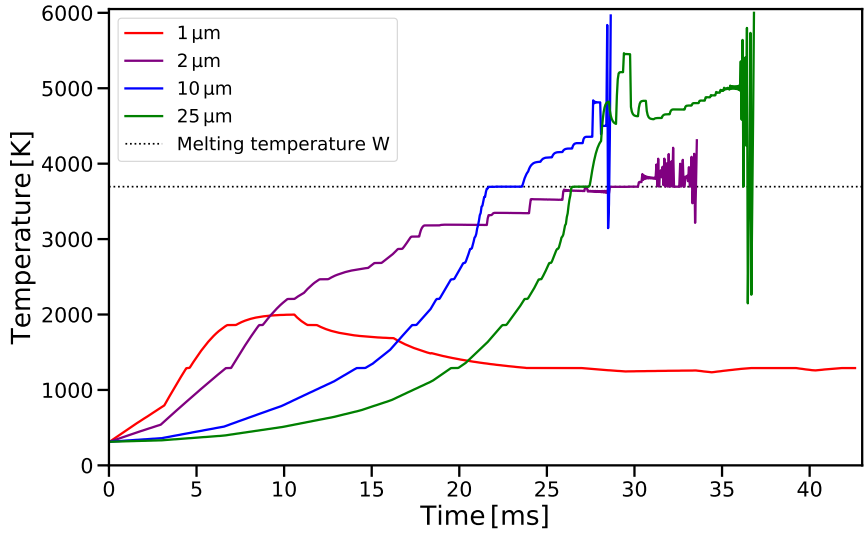

FIGURE 6.6: Temperature of the grains obtained from the simulation. For the 2 μm, 10 μm and the 25 μm grain they are evaporated after the last data point. The 1 μm grain does not evaporate. The color code is the same as in figure 6.5.

evaporate before they reach the separatrix. For the 25 μm grain this leads to a significant mass release in the separatrix region and even inside it but the limits of the code in this region do only allow an estimation. Other sources of uncertainty regarding the plasma background will be discussed later.

For the 25 μm grain also the contribution of the forces to the acceleration of the grain is shown to illustrate which forces have a high impact on the motion of the dust grain. The corresponding development of the forces can be found in the Appendix in figure B.4. The plot of the magnitude of the acceleration for the 25 μm grain in figure 6.8 illustrates the main contributions of the ion drag and the gravitational force. Towards the end close to the point of evaporation the contribution of the rocket force increases as the magnitude of the rocket force is dependent on temperature of the grain. Overall the trajectory of the grain does only get altered little by the plasma as the comparison to the 2 μm grain in figure 6.4a shows.

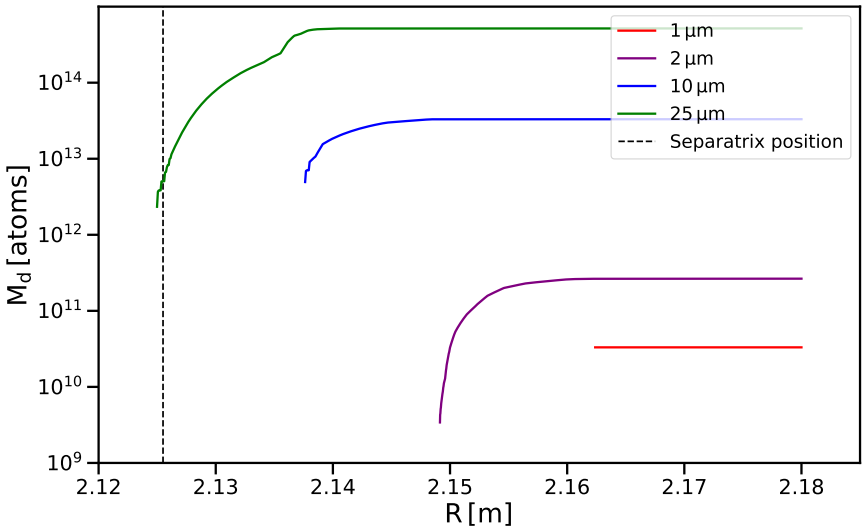

FIGURE 6.7: Mass of the grains over the radial coordinate of AUG. The last shown mass for the 2 μm, 10 μm and 25 μm grain is the mass one time step before the grains evaporate. The color code is the same as in figure 6.4.

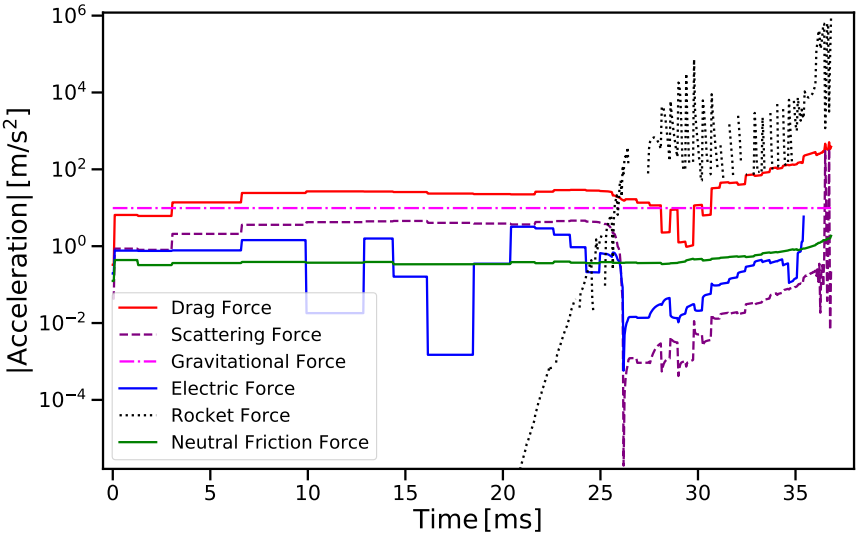

FIGURE 6.8: Acceleration of the 25 μm grain with injector velocity due to the different forces that are implemented in DUCAD. The last data point is obtained in the time step before the grain is evaporated.

6.2.2 Modelling of faster particles

Additionally, to the modelling using the parameters of the injector, a different initial velocity is considered. The velocity of the injected particles of the injector are at the lower end of the observed velocities resulting from arcing. Therefore, in this section grains with a velocity of $10\,\mathrm{m\,s^{-1}}$ are considered. This is still at the lower end of observed velocities [12, 31] or velocities of particles created by arcing [10, 13] but significantly higher than the velocity of the injector. The calculation is done with the same time step of $50\,\mu\mathrm{s}$.

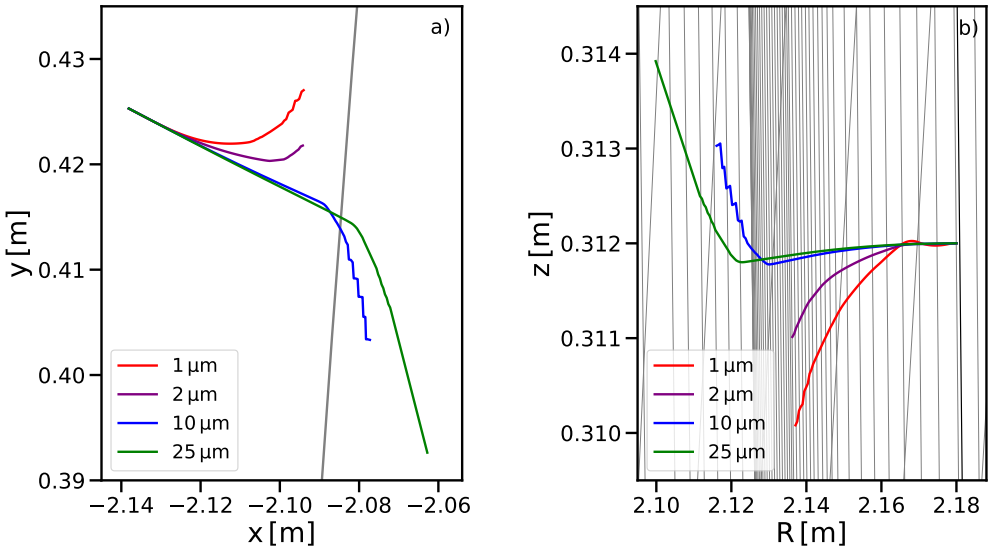

FIGURE 6.9: (a) Close view on the toroidal projection of the trajectories calculated with DUCAD. The grey circle indicates the approximate separatrix position at the height of the injector. (b) Close view on the poloidal projection of the trajectories of the DUCAD simulation in the AUG tokamak. The marking on the y-axis at 0.312 m indicates the position of the injector. The range of the y-axes is smaller than that in figure 6.4. The color code is the same as in figure 6.4.

Compared to the previous case all trajectories approach the separatrix and all particles evaporate or the calculation stops by reaching a limit of the code. In comparison to the previous case the ranges of the y-axes in figure 6.9 are smaller whilst the x-axes have similar ranges. This means that the observable displacements in figure 6.9 are smaller than in the previous case. The $1\,\mu$m and $2\,\mu$m grains have a larger toroidal displacement compared to the larger grains but much less than in the previous case. With a higher velocity the plasma force acting on all grains have less impact on the trajectory. The small grains are still affected by the forces acting on them whilst the other grains are almost not affected by the plasma forces. The trajectories end when the particle evaporates. The $2\,\mu$m shows less toroidal and poliodal displacement but does not get closer to the separatrix than the $1\,\mu$m grain. Both get closer to the

separatrix compared to the injector case with the lower velocity investigated before. The larger grains do not show a displacement until they get to the separatrix. The motion of the 10 μm grain is strongly altered when it is near and beyond the separatrix which is in a region of limited validity of the code. This also applies for the trajectory of the 25 μm grain inside and close to the separatrix. The grains with a diameter of 10 μm and 25 μm evaporate after crossing the separatrix and release W inside of the core plasma. Both trajectories can be considered accurate outside the separatrix. By approaching the separatrix the neglected effects like an ablation cloud can lead to breaking the assumptions of the OML approach. As those grains have a velocity in almost radial inward direction before reaching the separatrix and the calculated trajectories are inside of it, it is reasonable to assume that the particles will penetrate the separatrix.

The velocity of the 1 μm and 10 μm grains does increase significantly only just before the evaporation as shown in figure 6.10. The other grains do not show an increase in the velocity. The velocity is almost unchanged from the initial velocity in the beginning. The temporal evolution of the radius and velocity of the grains can be found in figure 6.10.

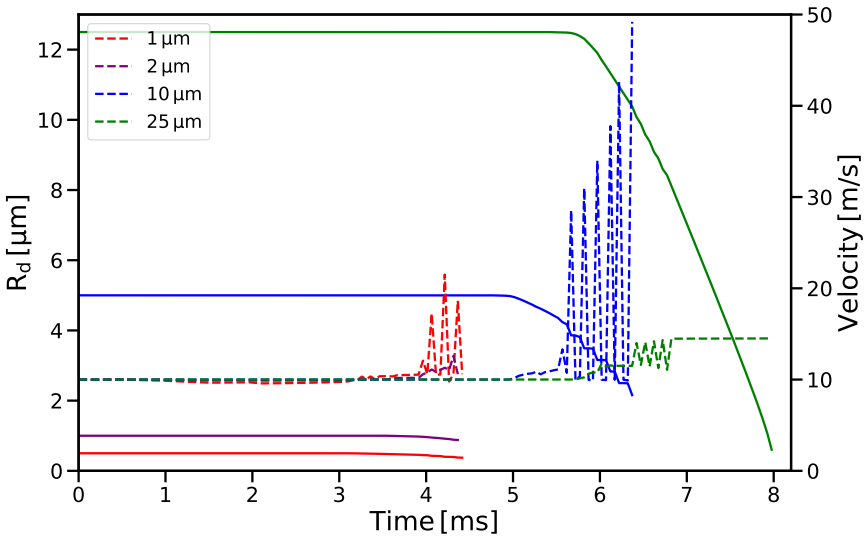

FIGURE 6.10: Development of the grain radius (solid) and the grain velocity (dashed) as a function of time after injection. The last radius or velocity of the grains is the one, one time step before the grain is evaporated. The color code is the same as in figure 6.9.

The development of the grain temperatures is illustrated in figure 6.11. The 1 μm and 2 μm show a faster temperature increase than the two larger grains. Due to the larger velocity the grains reach regions with higher plasma temperature earlier than in the previous case. This explains the faster increase of the grain temperature. For all grains the transition from a solid to a liquid grain

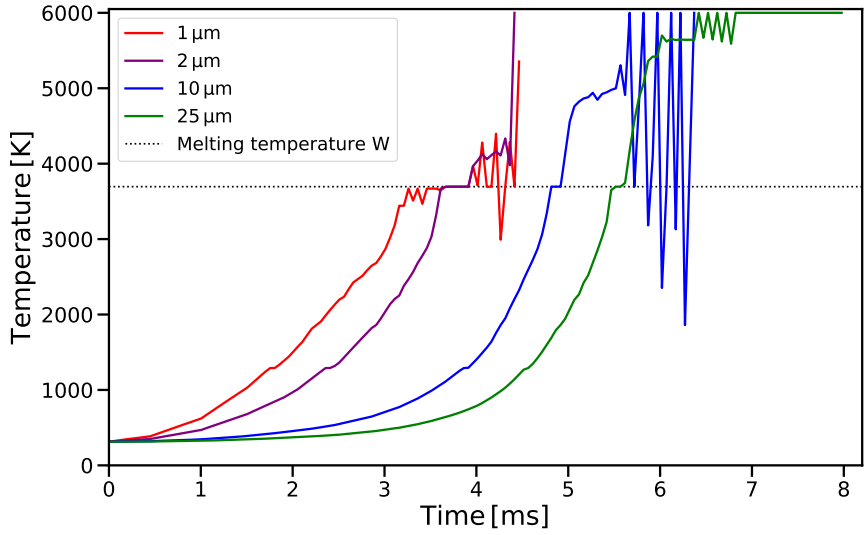

FIGURE 6.11: The temperature of the grains obtained from DUCAD. All grains have evaporated after the last data point. The color code is the same as in figure 6.9.

can be observed at the melting temperature by the step in the temperature plot.

The 25 μm grain reaches a temperature of 6000 K when crossing the separatrix which is the highest temperature calculated by the code. Further heating would lead to a fast evaporation of the grain. The 10 μm also reaches temperatures of 6000 K multiple times before the grain evaporates. Due to the restrictions of the code and focus on the SOL region the calculation in this region is not accurate. Limitations arise also by the neglected impact of the ablation cloud on the background plasma.

The mass loss of the grains along the radial coordinate is shown in figure 6.12. The 1 μm and 2 μm grains in this case approaches the separatrix but evaporate before they reach it. The 10 μm and 25 μm grains evaporate inside the separatrix position of the calculation grid but the data is prone to uncertainties. Those particles release almost all of their mass inside the separatrix as their mass loss of the grains before crossing the separatrix is small.

All particles penetrate further than in the previous case with the injector properties. For higher velocities the penetration depth increases as well as when considering larger grains but by the limitations of the code only the trajectory up to the start of the evaporation provides accurate and reliable results. After the onset of the evaporation which depends on the grain size and velocity the results are an estimation and approximation of the real behaviour especially when the ablation gets stronger when approaching the separatrix.

For the 25 μm grain the forces and the resulting acceleration are investigated. The acceleration of the grain is shown in figure 6.13 and the corresponding forces are depicted in figure B.6. As observed before the temperature

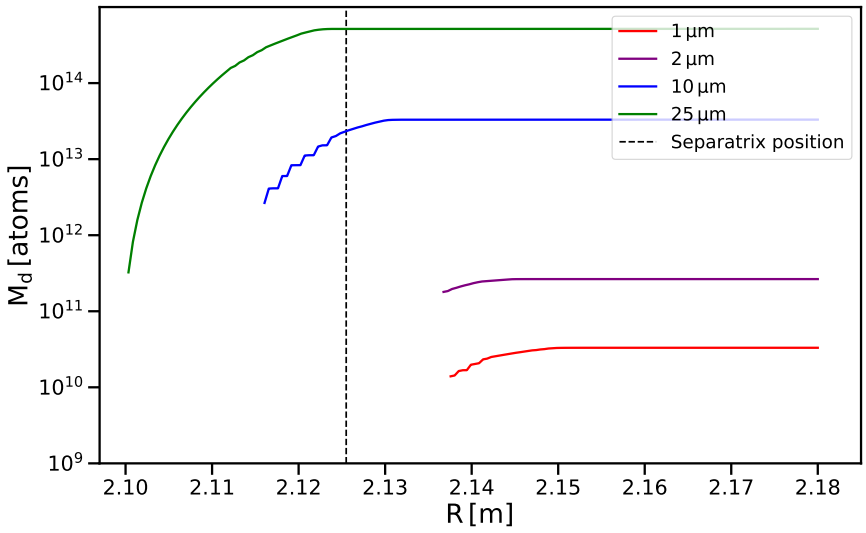

FIGURE 6.12: Mass of the grains over the radial coordinate of AUG. The last masses of the grains are the ones one time step before the grain is evaporated. The color code is the same as in figure 6.9.

reaches 6000 K and the obtained data is not accurate. Shortly before this temperature is reached the main acceleration originates from the rocket force. The drag force results in the highest acceleration from the injection on until it is exceeded by the rocket force.

6.3 Possible differences to experiment

Differences of the trajectories from these simulations to an injection in AUG may occur due to idealised grain shape, having a plasma background unaffected by the W release as well as the limitations of the code. Some of those restrictions were not relevant because for the comparison of the simulation with real trajectories these were in the SOL region and the effects have a lower impact.

The shape of the particles will influence the direction of the rocket force acting on the particles due to the complicated geometry which is neglected by calculating with spherical particles.

The plasma discharge used as background in this simulation with DUCAD is a L-mode discharge but a high power H-mode discharge will be used in the experiment. For a high power H-mode the power flux and density in the SOL is much higher leading to higher erosion of the particle.

In a real plasma discharge in comparison to the background plasma used for the calculation the plasma parameters are changing. This has an effect on the temporal evolution of the separatrix position as well as the plasma parameters like temperature and density. Further, a different discharge will

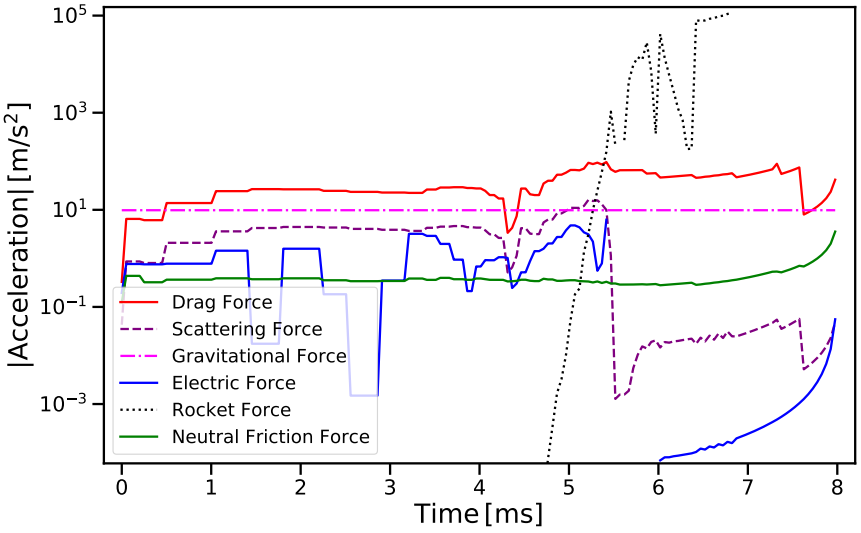

FIGURE 6.13: Acceleration of the 25 μm grain by the different forces calculated. The last data point of the grain is the one one time step before the grain is evaporated.

likely have a different separatrix position compared to the one considered in the simulations before. Grains getting to the separatrix in the simulation may or may not reach the separatrix for an injection into the plasma. Therefore, the previously mentioned separatrix position is only an approximate one as reference for the penetration depth.

This plays a larger role for the particles from the injector as their trajectories are influenced more by the forces acting on them and they are longer in the plasma environment until reaching the separatrix region.

The particles injected with a velocity of $10\,\mathrm{m\,s^{-1}}$ are less effected by the forces acting on them. In comparison to the injector case the toroidal and poloidal displacement is smaller which shows the effect of the initial velocity. The large grains will most likely be not affected much by different parameters and even faster particles will travel almost unaffected by the plasma.

The velocity behaviour and trajectory of the particles will be measured by fast cameras during the plasma experiment and can be used as input and comparison for simulations.

High gradients in the separatrix region and the constant time step in the simulation code lead to inaccurate results in this region which results in strongly varying values as seen for the temperature, acceleration and partly the velocity.

Following this the simulation handles one single grain but the injector as seen before has an injection mass of 565 μg per injection. Assuming only spherical grains with a diameter of 25 μm each grain has a mass of 0.16 μg and contains 5.2×10^{14} atoms. With this estimation one injection would contain 3600 particles which illustrates the difference of simulation and experiment. This will have an effect on the surrounding plasma and will alter the plasma

in the SOL. Those effects are not included in the calculation of a single grain.

Following the simulation, the large grains of the powder ejected by the injector have the probability to penetrate the separatrix. The injector is capable to inject particles close to the separatrix where they evaporate and release W. Additional effects such as an ablation cloud and especially the much higher number of particles will play a role. The penetration probability for particles with a velocities of $10\,\mathrm{m\,s^{-1}}$ is higher. The trajectory for the large grains are almost not influenced by the plasma.

Chapter 7

Conclusion

A particle injector supplied from the Korean tokamak KSTAR was successfully taken into operation. After initial testing and optimisation a reliable operation was ensured and the injector was installed at AUG.

The idea with the injector at AUG was to inject known amounts of characterised W powder to evaluate the change of the core W concentration. From the experiments the penetration probability of different W particles and powders could be determined. This allows conclusions about the effect of intrinsic W dust in the machine. With fast cameras the trajectory of the injected particles can be tracked to gain information about the transport of the dust in the machine.

The characteristics of the injection were determined. The mass per injection was evaluated for different powders and showed the dependence of the injected mass on the powder as well as the influence of the loading mechanism of Injector A. The parameters of the injection like initial velocity and cloud shape were evaluated by recording the injected dust cloud with a fast camera and analysing the recordings. For the illumination of the dust different methods were tested. The evaluation of the initial velocity at atmospheric pressure and under vacuum condition showed small differences but the evolution was different. Further, the achieved ranges were shorter due to the friction in air. In vacuum a compact dust cloud was observed whereas in air the spread of the cloud was much larger. The investigation of the injection in vacuum was an extension to the characterisation done in Korea. The exchangeable spring allows injections with different characteristics which in conjunction with different powders allows to perform a variety of experiments in the future. This would require additional characterisations of the properties for different combinations of spring and powder.

The characteristics of the investigated injector fulfil all mechanical and injection properties required for the installation and operation at AUG. The device was mounted on the MEM of AUG, however experiments were not possible, since the operation was delayed after a steam leak and the necessary repairs.

Instead, the penetration of the injected particles was studied using the

characterisation of the injection as input parameter for the simulations of the dust trajectory in the plasma. The DUCAD code was applied to calculate the trajectories of dust grains. The simulations showed a clear dependence of the penetration on the size of the grain as well as on its initial velocity. For injections with the determined initial properties of the injector only the largest grains simulated come close to the separatrix and evaporate. Small grains get accelerated back to the wall and do not show any penetration probability. With a higher velocity the large grains evaporate inside the separatrix and the small grains also penetrate deeper than for the simulations with injector properties.

Differences between code and experiments are expected due to temporally changing plasma parameters compared to the constant modelled plasma background and the much larger mass and particle number per injection compared to the single grain simulated.

Nevertheless, the comparison of the experimental data with simulations can help to further improve the modelling and simulations of dust transport in the future. The characterised initial conditions of the injector are known. The interaction with the plasma can be measured during experiments. Combined they provide a large data set with only few variables unknown that can be used for accurate simulations and code improvements.

Appendix A

Evaluation method and threshold choice

During the description of the video evaluation two methods were mentioned. One tracking all dust above a certain threshold and one tracing the most forward particles. Further, the influence of the threshold was discussed and its impact on the trajectory evaluated. The plots of the comparison of the method as well as of the threshold are shown here for better illustration.

Figure A.1 illustrates the difference of the choice of the tracking method.

Figure A.2 shows the difference of the limit on the fitted trajectory and the included pixels. The tracked dust positions in figure A.2a at the start below the trajectory are part of the lower cloud portion that with increasing time is behind the traced front particles, shows lower signal intensity and therefore is not considered with the front tracking method. Moreover, this can be observed in figure A.1a in which the method tracking all dust also traces the particles of the lower cloud portion. The front method only traces a small portion of the front of the lower portion as the upper part is farther in injection direction and is therefore traced.

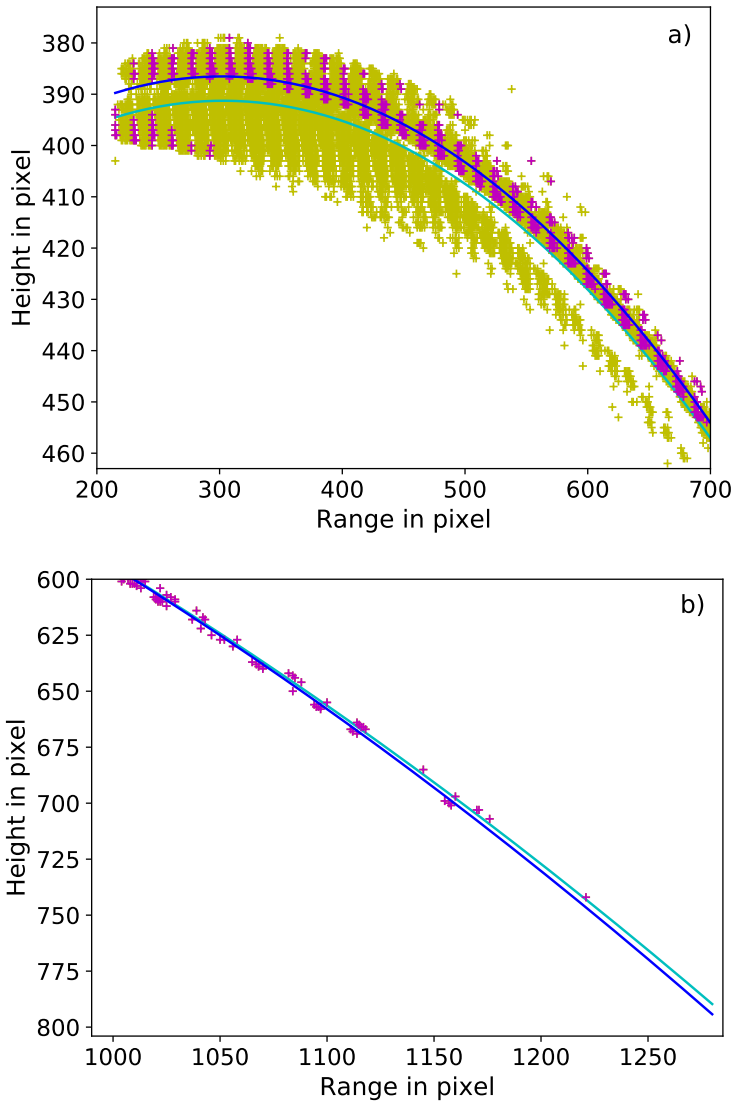

FIGURE A.1: The plots show the difference of the tracking methods close to the injector in (a) and towards the end of the observed image section in (b). The picture shows the dust signal for each frame superimposed. The yellow points are obtained by plotting all points above the limit and the cyan fitted trajectory is the respective fit to the mean position of each frame. The blue fit and the magenta points are obtained from the front method. The method considering all points is lower in the beginning as also particles of the lower cloud part contribute. Later both methods contain the same points when the overall number is below the criterion for the front. Due to the initial difference the trajectories also vary at the end. The limit chosen for both methods is the same. The distances on the axes are given in pixels and can be converted by multiplying by $0.198\,\mathrm{mm\,px^{-1}}$.

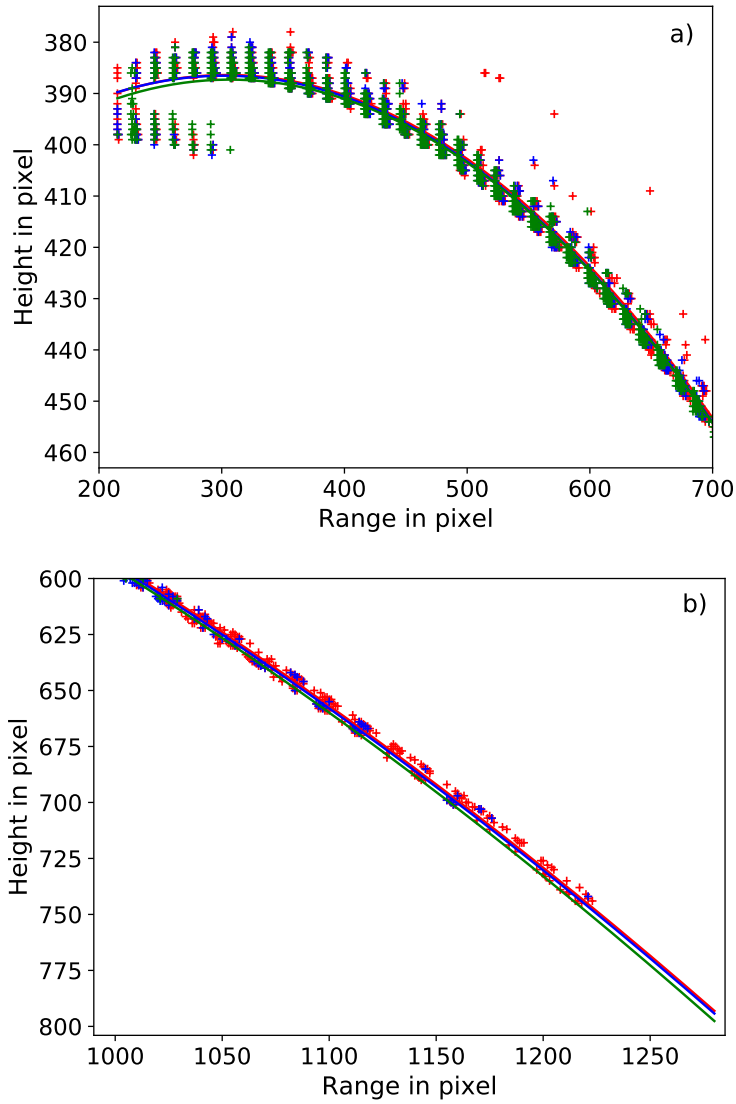

FIGURE A.2: The trajectories shown in the picture are found by fitting a quadratic function to the points found by tracking the 25 most forward pixels above the intensity threshold chosen for the dust. The middle, blue trajectory is obtained by applying a threshold. The red one above it has a lower threshold and the green one below has a higher threshold. Points and fits of the same colour belong to each other. The difference of the higher and lower threshold from the middle one is the same. The injection analysed was an injection in the chamber under vacuum conditions. Shown in (a) is a zoom on the region close to the injector and (b) is a zoom in on the last part of the trajectory. The distances on the axes are given in pixels and can be converted by multiplying by $0.198\,\mathrm{mm\,px^{-1}}$.

Appendix B

Additional simulation plots

In the following there are additional plots to illustrate the position of the injector and the trajectory of the dust in the device. Additionally, 3D plots of the trajectories are given. To extend the shown plot of the accelerations of the grains here the different forces on the grain are given. Figures B.1 and B.2 show the complete the toroidal and poloidal cross section of AUG with the calculated trajectories of the injector. The close view on the trajectories is in found in chapter 6 in figure 6.4.

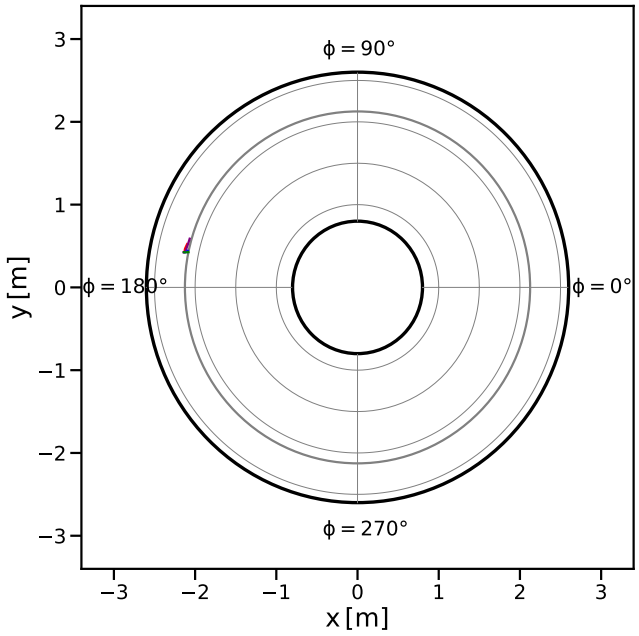

FIGURE B.1: Toroidal, top view of the trajectories calculated with DUCAD. The 1 μm grain in red, the 2 μm one in purple, the 10 μm in blue and the 25 μm one in green. The grey circle indicates the separatrix position at the height of the injector. The inner black circle is the position of the inner wall and the outer black circle is the outer wall of the vacuum vessel.

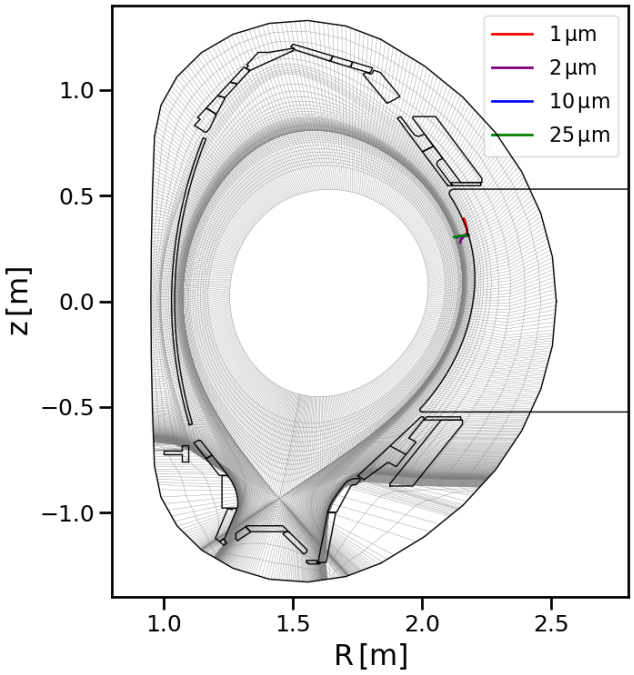

FIGURE B.2: Projection of the trajectories of the DUCAD simulation in the poloidal plane of the AUG tokamak. The grains are delivered by the injector. The 1 μm grain in red, the 2 μm one in purple, the 10 μm one in blue and the 25 μm one in green.

Figure B.3 shows a 3D plot of the trajectories for the injection with the injector.

Figure B.4 illustrates the forces acting on the simulated 25 μm grain for a particle simulated with initial properties of the injector.

A 3D plot of the trajectories for an injection with 10 m s^{-1} initial velocity is shown in figure B.5.

Figure B.6 illustrates the forces acting on the simulated 25 μm grain calculated with a velocity 10 m s^{-1}.

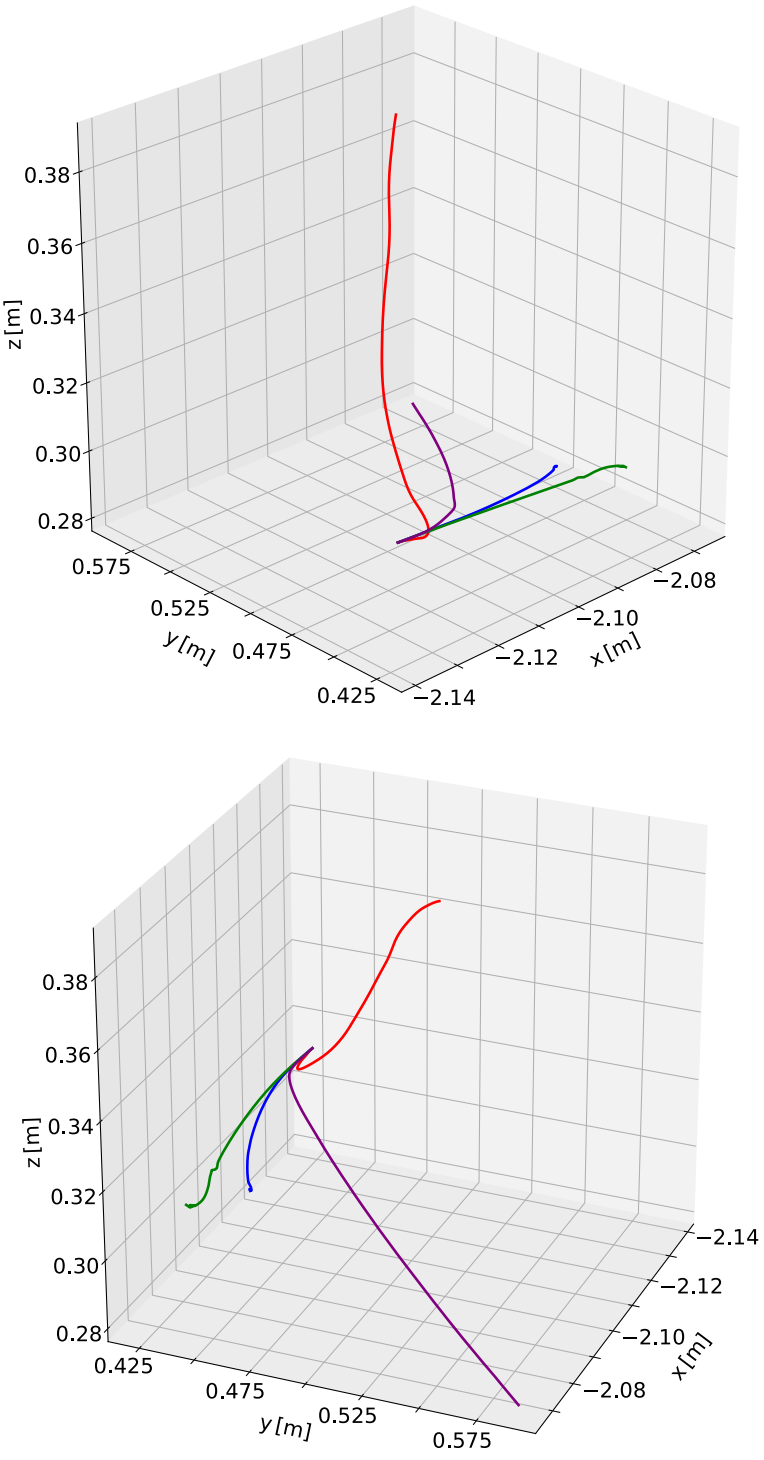

FIGURE B.3: 3D plots of the trajectories viewed in direction of the initial velocity. The 1 μm grain in red, the 2 μm one in purple, the 10 μm in blue and the 25 μm one in green.

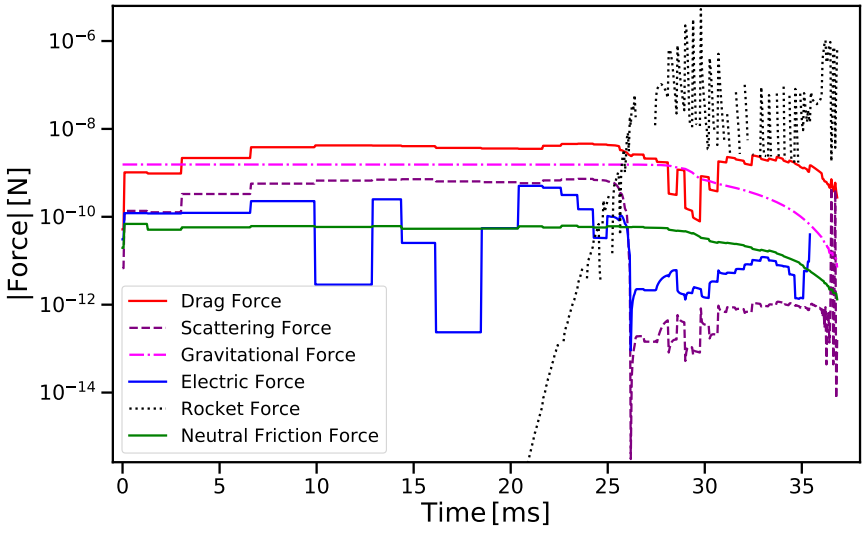

FIGURE B.4: Evolution of the forces that are implemented in DUCAD acting on the grain 25 μm for simulated for the injector. The last data point is obtained in the time step before the grain is evaporated.

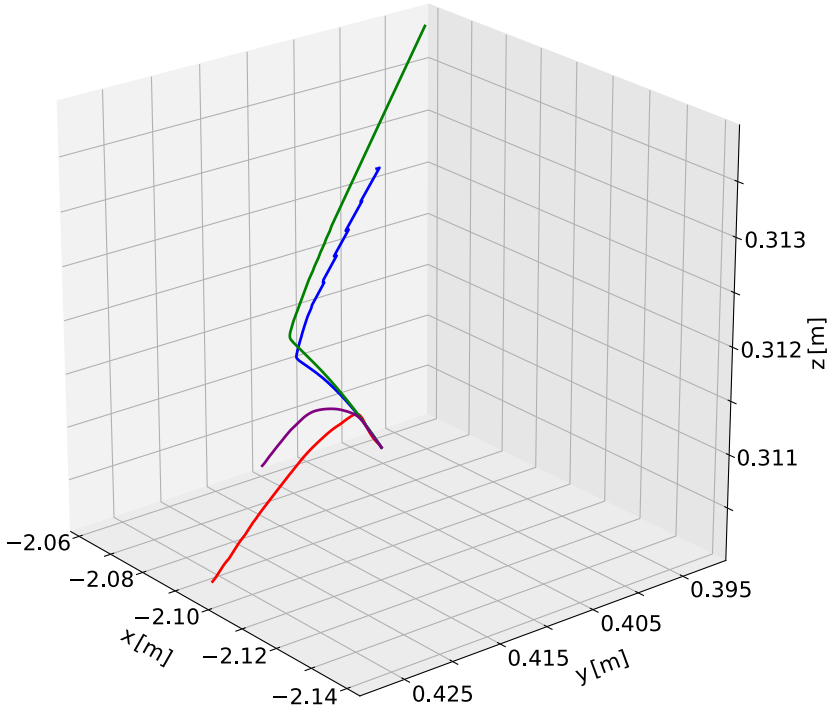

FIGURE B.5: 3D plots of the trajectories obtained from simulations with an initial velocity of 10 m s^{-1}. The 1 μm grain in red, the 2 μm one in purple, the 10 μm in blue and the 25 μm one in green.

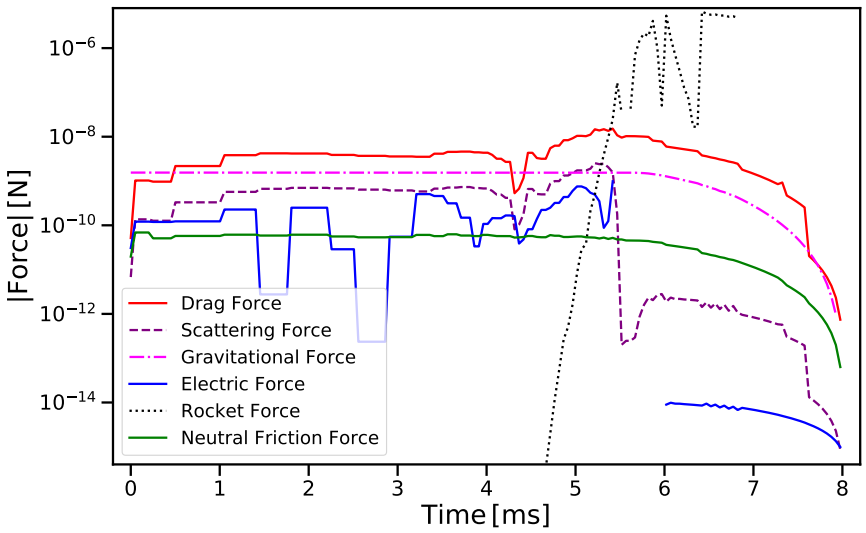

FIGURE B.6: Evolution of the forces acting on the grain 25 μm calculated with an initial velocity of 10 m s^{-1}. The last data point is obtained in the time step before the grain is evaporated.

Bibliography

[1] International Fusion Research Council (IFRC), Nuclear Fusion **45**, A1 (2005).

[2] R. Pampin *et al.*, Fusion Engineering and Design **87**, 1230 (2012).

[3] A. C. C. Sips *et al.*, Physics of Plasmas **22**, 021804 (2015).

[4] U. Stroth, *Plasmaphysik*, 2. Auflage, Springer Spectrum, 2018.

[5] T. Pütterich *et al.*, Nuclear Fusion **50**, 025012 (2010).

[6] A. Autricque *et al.*, Nuclear Materials and Energy **12**, 599 (2017).

[7] H. Y. Lee *et al.*, Review of Scientific Instruments **85**, 11D862 (2014).

[8] G. Federici *et al.*, Nuclear Fusion **41**, 1967 (2001).

[9] D. L. Rudakov *et al.*, Review of Scientific Instruments **79**, 10F303 (2008).

[10] V. Rohde, M. Balden, T. Lunt, and the ASDEX Upgrade Team, Physica Scripta **2009**, 014024 (2009).

[11] D. Rudakov *et al.*, Journal of Nuclear Materials **438**, S805 (2013).

[12] S. I. Krasheninnikov, R. D. Smirnov, and D. L. Rudakov, Plasma Physics and Controlled Fusion **53**, 083001 (2011).

[13] M. Balden *et al.*, Nuclear Fusion **54**, 073010 (2014).

[14] F. Brochard *et al.*, , Nuclear Materials and Energy (submitted 2018).

[15] R. Smirnov *et al.*, Journal of Nuclear Materials **390-391**, 84 (2009).

[16] D. Rudakov *et al.*, Nuclear Fusion **49**, 085022 (2009).

[17] S. I. Krasheninnikov *et al.*, Plasma Physics and Controlled Fusion **50**, 124054 (2008).

[18] S. Ratynskaia, C. Castaldo, H. Bergsåker, and D. Rudakov, Plasma Physics and Controlled Fusion **53**, 074009 (2011).

[19] R. D. Smirnov, S. I. Krasheninnikov, A. Y. Pigarov, and T. D. Rognlien, Physics of Plasmas **22**, 012506 (2015).

[20] J. Roth *et al.*, Journal of Nuclear Materials **390-391**, 1 (2009).

[21] M. Shimada *et al.*, Journal of Nuclear Materials **438**, S996 (2013).

[22] T. Pütterich *et al.*, Plasma Physics and Controlled Fusion **55**, 124036 (2013).

[23] C. Angioni *et al.*, Nuclear Fusion **57**, 056015 (2017).

[24] N. Endstrasser *et al.*, Physica Scripta **2011**, 014021 (2011).

[25] N. Endstrasser *et al.*, Journal of Nuclear Materials **415**, S1085 (2011).

[26] J. Sharpe *et al.*, Journal of Nuclear Materials **313-316**, 455 (2003).

[27] J. P. Sharpe *et al.*, Journal of Nuclear Materials **337-339**, 1000 (2005).

[28] M. Shimada *et al.*, Nuclear Fusion **47**, S1 (2007).

[29] V. Rohde *et al.*, Journal of Nuclear Materials **415**, S46 (2011).

[30] V. Rohde, M. Balden, N. Endstrasser, and U. von Toussaint, Journal of Nuclear Materials **438**, S800 (2013).

[31] F. Brochard *et al.*, Nuclear Fusion **57**, 036002 (2017).

[32] S. Hong *et al.*, Nuclear Instruments and Methods in Physics Research Section A: Accelerators, Spectrometers, Detectors and Associated Equipment **720**, 105 (2013).

[33] A. Shalpegin *et al.*, Plasma Physics and Controlled Fusion **57**, 125017 (2015).

[34] J. Yu *et al.*, Journal of Nuclear Materials **390-391**, 216 (2009).

[35] R. D. Smirnov *et al.*, Plasma Physics and Controlled Fusion **51**, 055017 (2009).

[36] S. Ratynskaia *et al.*, Nuclear Fusion **53**, 123002 (2013).

[37] A. Litnovsky *et al.*, Journal of Nuclear Materials **438**, S126 (2013).

[38] K. Krieger *et al.*, Physica Scripta **2011**, 014067 (2011).

[39] D. Rudakov *et al.*, Journal of Nuclear Materials **363-365**, 227 (2007).

[40] G. Raupp *et al.*, Fusion Engineering and Design **66-68**, 947 (2003).

[41] https://www.aug.ipp.mpg.de/aug/local/aug_only/vacuum_vessel/Labor1.html last visited: 25.08.2018.

[42] K. Krieger *et al.*, Journal of Nuclear Materials **415**, S297 (2011).

[43] T. Lunt *et al.*, Journal of Nuclear Materials **415**, S505 (2011).

[44] G. S. López, Master's thesis, University of Lorraine, 2015.

[45] M. Bacharis, M. Coppins, and J. E. Allen, Physics of Plasmas **17**, 042505 (2010).

[46] A. Y. Pigarov, S. I. Krasheninnikov, T. K. Soboleva, and T. D. Rognlien, Physics of Plasmas **12**, 122508 (2005).

[47] L. Vignitchouk, P. Tolias, and S. Ratynskaia, Plasma Physics and Controlled Fusion **56**, 095005 (2014).

Danksagung

An dieser Stelle möchte ich mich bei allen bedanken, die mir während der Forschungsphase und der Masterarbeit geholfen haben.

Mein besonderer Dank gilt Volker Rohde, der sich immer Zeit für meine Fragen und Probleme nahm, ob technisch, physikalisch oder bei der wissenschaftlichen Formulierung dieser Arbeit und diese Arbeit initiiert hat.

Vielen Dank an Rudolf Neu für das Ermöglichen meiner Masterarbeit, der Teilnahme an der DPG Frühjahrstagung und die hilfreichen Anmerkungen beim Anfertigen dieser Arbeit.

Dank gilt auch meinen Bürokollegen Thomas Reichbauer, Klara Höfler und Johannes Illerhaus für die angenehme Arbeitsatmosphäre, deren Hilfe bei diversen technischen und physikalischen Fragen und zahlreiche interessante Diskussionen. Danke sagen möchte ich auch Stephan Glöggler, Lennart Bock, Michael Griener und Felician Mink für spontane Hilfe bei physikalischen und technischen Problemen und die Hilfe bei der Einarbeitung ins System.

In Bezug auf den Mittelebenen Manipulator gilt mein Dank Dominik Brida für das Organisieren des Einbaus des Injektors sowie Pascal de Marné für die Hilfe beim Positionieren des eingebauten Injektors für Fotos.

Weiter möchte ich mich bei den Kollegen des Vakuumlabors, im besonderen Detlef Bösser, für die Hilfe bei Arbeiten an der Vakuumkammer bedanken . Weiter geht mein Dank an Peter Leitenstern für das Anfertigte der nötigen CAD Zeichnungen für Änderungen an Injektor Bauteilen. In diesem Sinne möchte ich auch dem Team der Werkstatt, besonders Karl Eismann, für die schnelle Bearbeitung sowie der Elektronik Werkstatt für die ausgeführten Arbeiten danken.

Ein besonderer Dank geht an Guillermo Suárez López für das bereit stellen des DUCAD Codes, die Einführung in den Code sowie die Diskussion der Ergebnisse.

Ein weiterer Dank gilt des Weiteren allen, die an AUG den laufenden Betrieb und die Experimente ermöglichen und sich persönlich für mich Zeit nahmen.

Abschließend gilt mein großer Dank meiner Familie, die mich auf meinem Lebensweg immer unterstützt hat, meinen eigenen Weg zu finden und zu gehen.